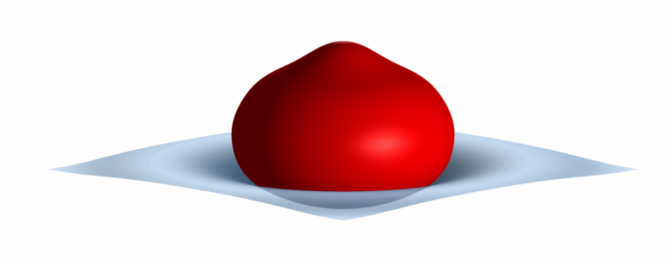


# Air entrainment during impact onto a liquid pool

MSc. Thesis Applied Physics  
Physics of Fluids, Faculty TNW  
University of Twente



June 22, 2013

*Author:*  
M.H.W. Hendrix

*Committee:*  
Prof. Dr. D. Lohse  
Dr. Ir. J.H. Snoeijer  
MSc. W. Bouwhuis  
Prof. Dr. R.M. van der Meer  
Dr. P.A. Tsai  
Dr. M.M.J. Dhallé



# Abstract

When a mm-sized drop approaches a liquid pool, both interfaces deform before the drop actually touches the pool. The build up of air pressure prior to coalescence is responsible for this deformation. Due to this deformation, air is usually entrained during impact. We quantify the amount of entrained air numerically, using the Boundary Integral Method (BIM) for potential flow for the drop and the pool, coupled to viscous lubrication theory for the air film that has to be squeezed out during impact. We compare our results to various experimental data and find excellent agreement in the amount of air that is entrapped during drop impact onto a pool. Also the impact of a rigid sphere onto a pool is numerically investigated and the air that is entrapped in this case also matches with available experimental data. In both cases of drop and sphere impact onto a pool the numerical air bubble volume  $V_b$  that is found is in agreement with the theoretical scaling  $V_b/V_{drop/sphere} \sim St^{-4/3}$ , where  $St$  is the Stokes number. This implies a universal mechanism for air entrainment for both impact scenarios, which has been suggested in recent experimental work, but can now be further investigated with numerical results. In addition, experiments have been conducted to infer the dynamics of a thin air film that is entrapped between an impacting drop and a hydrophobic micro structure using high speed color interferometry.



# Contents

<b>1</b>	<b>Introduction</b>	<b>5</b>
1.1	General introduction . . . . .	5
1.2	Thesis structure . . . . .	6
<b>2</b>	<b>Background</b>	<b>7</b>
2.1	Drop impact onto a solid plate . . . . .	7
2.2	Dimple characterization . . . . .	8
2.3	Impact onto a pool . . . . .	9
<b>3</b>	<b>Theory</b>	<b>11</b>
3.1	Boundary Integral Method for Potential flow . . . . .	11
3.2	Boundary conditions . . . . .	12
3.3	Lubrication approximation for Stokes flow . . . . .	13
3.3.1	Drop impact onto a flat surface . . . . .	13
3.3.2	Drop impact on a liquid pool . . . . .	14
3.4	Coupling air dynamics to the BIM . . . . .	17
<b>4</b>	<b>Air entrainment during solid sphere impact on a liquid pool</b>	<b>19</b>
4.1	Time evolution of sphere impact onto liquid pool . . . . .	20
4.2	Contact diameter at impact . . . . .	20
4.3	Entrapped air bubble volume . . . . .	20
<b>5</b>	<b>Drop impact onto a liquid pool</b>	<b>23</b>
5.1	Entrapped air bubble volume . . . . .	23
5.2	Experimental results: penetration depth viscous drop onto a pool . . . . .	30
<b>6</b>	<b>Air film dynamics during drop impact onto hydrophobic micro-patterned surfaces</b>	<b>32</b>
6.1	Experimental details . . . . .	32
6.2	Characteristics of airfilm . . . . .	33
<b>7</b>	<b>Discussion and outlook</b>	<b>37</b>
7.1	Discussion . . . . .	37
7.2	Outlook . . . . .	37
<b>A</b>	<b>Stokes flow in cylindrical coordinates</b>	<b>39</b>
<b>B</b>	<b>SRYL theory for slow drops</b>	<b>41</b>
	<b>Acknowledgments</b>	<b>44</b>
	<b>References</b>	<b>46</b>

# Chapter 1

## Introduction

### 1.1 General introduction

The impact of a spherical object onto a liquid pool is a fundamental problem in fluid physics, and was studied already in 1897 by A.M. Worthington and R.S. Cole. In their pioneering work [1, 2] they were able to freeze the motion of a sphere impacting onto a liquid pool with the help of instantaneous photography. A very precisely triggered  $3\text{-}\mu\text{s}$  duration spark with adjustable delay served as illumination to capture an individual image at a desired time during the impact event. An example of an image that they acquired is depicted in Fig. 1.1 a).

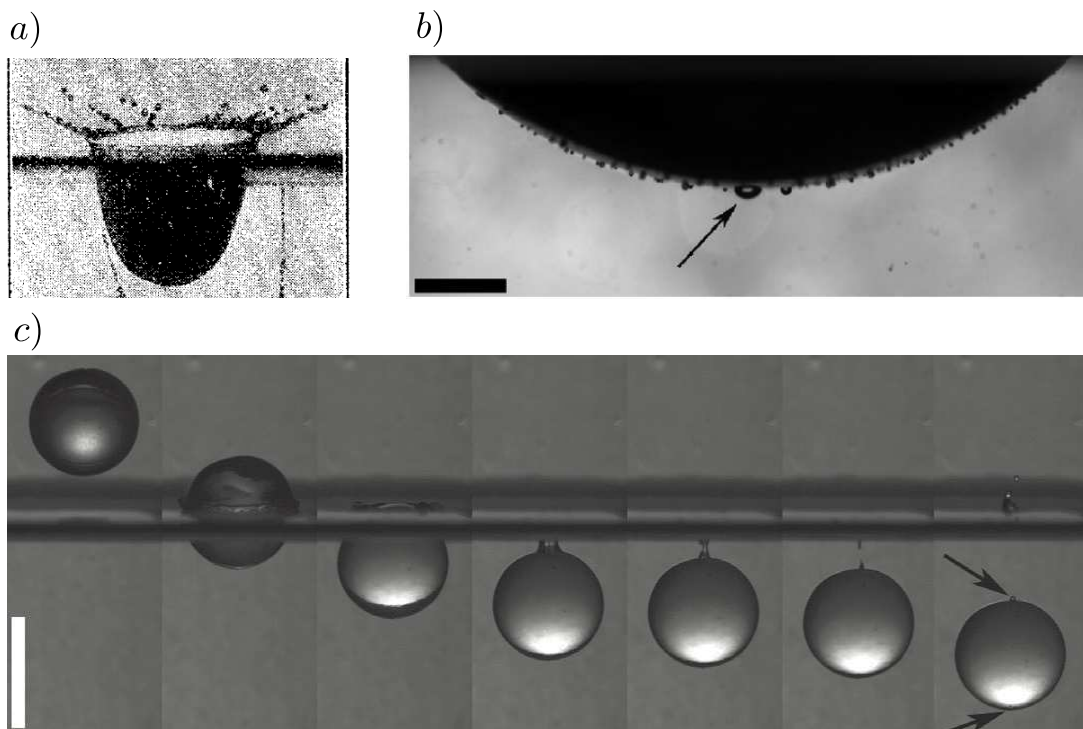


Figure 1.1: a) Photograph of an impacting sphere onto a liquid pool, courtesy of Worthington and Cole [2] b) Snapshot of air bubble entrainment of an impacting sphere onto a liquid pool, courtesy of Marston et al. [3] The scale bar is 2 mm. A central air bubble indicated with an arrow along with several satellite bubbles can be observed c) High-speed image sequence of an impacting sphere onto a liquid pool, courtesy of Marston et al. [3] Entrapped air bubbles are indicated with arrows in the final frame. The scale bar represents 1 cm.

With the advent of highspeed cameras these kind of impact phenomena, which typically take place on a millisecond time scale, can be studied in more detail. As was recently shown by Marston et al. [3], an impacting sphere entering a liquid pool can entrap air bubbles at the bottom of the sphere (see Fig. 1.1 b)

as well as at the apex of the sphere (see Fig. 1.1 c). The air entrainment mechanism of the latter case can be understood as follows: When an object falls onto a pool, it usually creates a cavity behind the object as a result of the fluid that is displaced during impact. The subsequent collapsing cavity can leave a trapped bubble at the rear of the object, as was also shown in [4, 5]. The mechanism of air entrainment at the bottom of the impacting sphere is quite different, as is sketched in Fig 1.2a. Due to the build up of air pressure the liquid pool deforms before the sphere actually touches the liquid, which results in an entrapped air bubble. Similar air bubble entrainment is observed when a liquid drop instead of a solid sphere falls onto a liquid pool [6, 7]. Also, due to the same local increase of pressure around the impact zone, air entrainment can be observed when a drop impacts onto a solid surface. [8]. These three different scenarios have been schematically depicted in Fig. 1.2

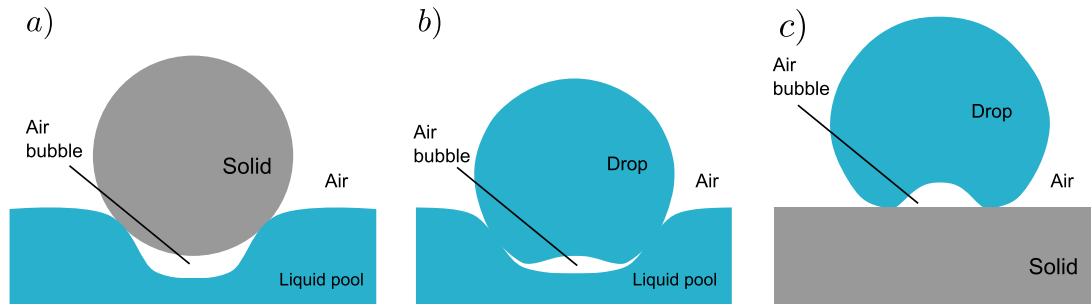


Figure 1.2: a) Rigid sphere impact onto a pool. The pool deforms due to an increase in air pressure right under the sphere before the sphere touches the pool, which results in an entrapped air bubble. b) Drop impact onto a pool. Not only the pool, but also the drop consists of a deformable interface. As a result, the increased air pressure deforms both the pool and the drop and an air bubble is entrapped. c) Drop impact onto a solid. Also here, a local increase in air pressure deforms the drop before it touches the solid and results in an entrapped air bubble

It is this mechanism of air entrainment that is the main focus of this thesis. The primary goal is to capture the essential physics of such an impact event into a numerical model. We will identify details of the pressure development in the air film and deformation of the interfaces at the impact zone. Quantitatively we will find out how the volume of the air bubble depends on several physical parameters such as impact velocity, and compare these results among the different scenarios depicted in Fig. 1.2. The results of the numerical model will be compared with available results from multiple experimental works. Considering the geometry of the problems described above, a 2d axisymmetric model can be used. In addition, to study the interplay of air and a drop during a more complex 3d problem, the air film under a drop and a micropatterned surface is experimentally investigated. The micropatterned surface is expected to have an influence on the dynamics, since the micro morphology of the surface is of the same size as the typical thickness of the air layer, as will become apparent. The outline of the thesis will be discussed in the next section.

## 1.2 Thesis structure

This thesis is organized as follows. In Chapter 2 a general background regarding the topic will be given. Chapter 3 covers the theory that is used in the numerical model. In this chapter we will see that the liquid phase will be modeled with a different technique compared to the approach that is taken to model the airflow. In Chapter 3.4 the coupling between the air layer and liquid phase is explained. Chapter 4 covers the numerical result of air entrainment during sphere impact onto a pool, and a comparison with available experimental data will be made. In Chapter 5 the slightly more complicated case of drop impact onto a pool will be discussed. Again a comparison between numerical results and experiments will be made. In Chapter 6 the experimental characterization of the air film dynamics under an impacting droplet onto a hydrophobic micro structure will be discussed. Chapter 7 will reflect on the content of this thesis, and opportunities for future research will be discussed.

# Chapter 2

## Background

This thesis concerns drop impact onto a flat plate, drop impact onto a liquid pool, and impact of a rigid sphere onto a liquid pool. Though these phenomena may seem quite different, the same physical mechanism is responsible for the initial deformation of the liquid interface: the build up of air pressure at the impact zone. In the current chapter this phenomenon is described by considering the extensively studied case of drop impact onto a flat plate as an example, and relevant dimensionless numbers for the problem will be identified.

### 2.1 Drop impact onto a solid plate

When a drop approaches a solid surface, the surrounding air will also be displaced by the moving drop. In the final stage of approach, a thin air layer between the solid and the drop needs to be squeezed out, see Fig. 2.1.

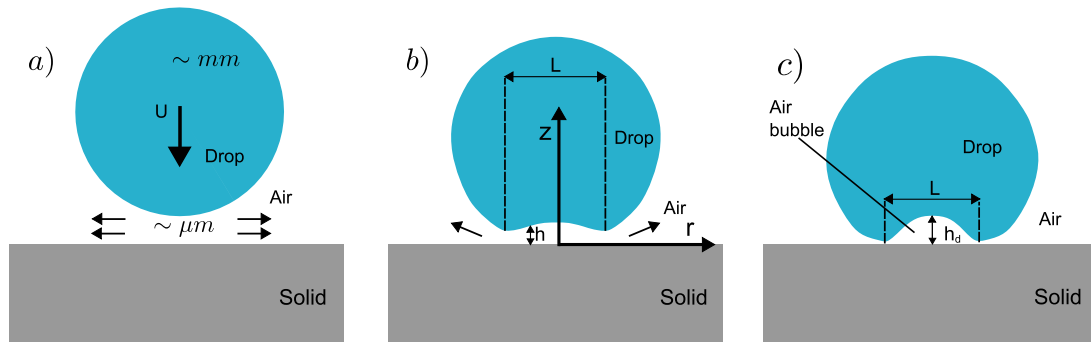


Figure 2.1: a) Schematic of  $mm$ -sized drop impact onto a solid surface. An air layer (with a typical thickness in the order of  $\mu m$ ) needs to be squeezed out when the drop is approaching the surface. b) Due to the increase of air pressure at the bottom of the drop a dimple is formed before the drop touches the surface. The air film which is trapped between the drop and the surface is characterized by a thickness  $h(r, t)$  and a lateral extension  $L$ . c) The drop touches at the thinnest point, thus entrapping air.

It turns out that this air film can influence the drop dynamics before the drop can actually touch the surface. This can be understood as follows: the pressure of the thin air film that is trapped will increase, and deform the interface locally. As a consequence a dimple can be formed at the bottom of the drop, see Fig. 2.1b. The location of the smallest separation distance between drop and solid is not located in the center anymore but at a rim position  $r > 0$ . Eventually the drop will touch the solid at this location, and will thus entrap an air bubble, see Fig. 2.1c. These collisions of drops with a solid surface and subsequent air entrapment have been recently quantified by Bouwhuis et al. [9], where  $mm$ -sized ethanol droplets impacting on a glass surface were studied. The experimental setup that was used is depicted in Fig. 2.2. A high speed color interferometry technique [10] was used to infer the dynamics of the microscopic air film just before the drop touches the surface, see Fig. 2.2c. This method uses the color information in the interference fringes to reconstruct the profile of the air film. It has become apparent now that quite different length scales are involved in the problem: while the size of impacting drops is in the order of

millimeters, the air film thickness is in the order of micrometers. In Chapter 6 this color interferometry method will be used to analyze the dynamics of the air film between an impacting drop and a structured surface, in which case the impact is not axisymmetric anymore.

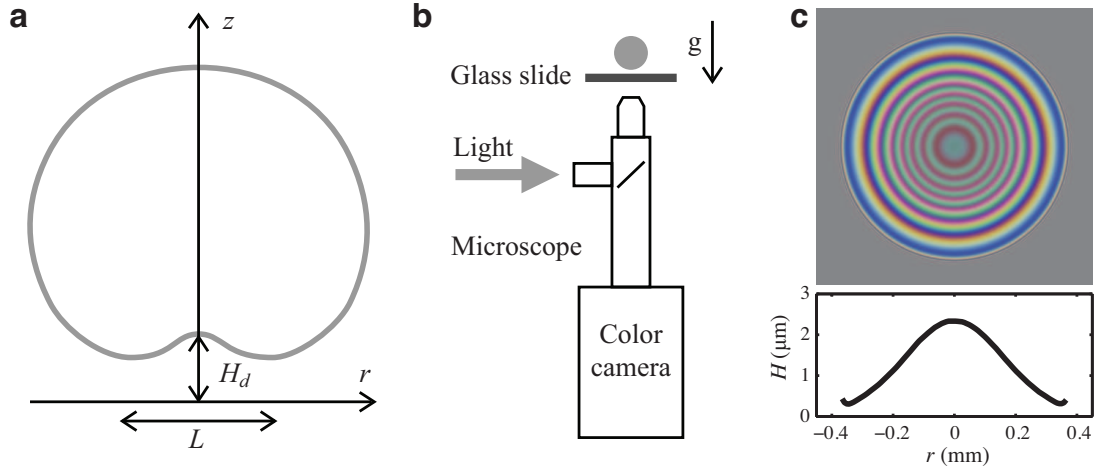


Figure 2.2: Taken from Bouwhuis et al. [9]. a) A sketch of dimple formation (not drawn to scale). The dimple is characterized by a dimple height  $H_d$  and a lateral extension  $L$ . b) A microscope is attached to a high speed camera to capture the interference fringes that originate from the thin air film that is trapped between the drop and the glass slide. c) An example of an interference pattern from which the air layer profile can be reconstructed.

Several relevant dimensionless numbers regarding the problem can be identified. The Reynolds number of the liquid drop  $Re_l \equiv \rho_l RU / \mu_l$  compares inertial forces to viscous forces in the drop. Here  $\rho_l$  and  $\mu_l$  are the density and viscosity of the liquid respectively.  $U$  is the impact velocity of the drop and  $R$  is the radius of the drop. This means that for high Reynolds number drops, the effect of viscosity can be neglected. The Reynolds number of the gaseous air layer  $Re_g$  is less obvious, because different length scales  $L$  and  $H_d$  (Fig. 2.1) are involved. From geometrical arguments it can be shown that  $L \sim \sqrt{H_d R}$  [9]. After analysis using a proper non-dimensionalized Navier-Stokes equation, see Appendix A, we identify the Reynolds number of the gas as  $Re_g \equiv \rho_g H_d U / \mu_g$ . Another important dimensionless group is the Stokes number  $St \equiv \rho_l RU / \mu_g$  which compares the viscous force of the air layer to the inertial force in the drop. This number is relevant for describing dimple formation, since, for high enough impact velocity  $U$ , dimple formation is determined by two competing forces: the force of the viscous air layer trying to deform the drop in the center opposing the inertial force of the drop, which needs to be slowed down locally in order to form a dimple. Additional dimensionless numbers incorporating surface tension  $\gamma$  are the Weber number  $We$  and Capillary number  $Ca$ , which are defined below. Summarizing we have the following dimensionless parameters:

$$Re_l \equiv \frac{\rho_l RU}{\mu_l} \quad Re_g \equiv \frac{\rho_g H_d U}{\mu_g} \quad St \equiv \frac{\rho_l RU}{\mu_g} \quad We \equiv \frac{\rho_l RU^2}{\gamma} \quad Ca \equiv \frac{We}{St}$$

## 2.2 Dimple characterization

The impact speeds considered in this thesis are at maximum in the order of  $m/s$ . Combining this with the fact that the thickness of the air film is in the order of  $\mu m$ , we can thus determine an upper bound for the Reynolds number of the gas:  $Re_g = \rho_g H_d U / \mu_g \sim 0.1$ , which shows that viscous effects are dominant compared to the inertial effects in the air film. This allows us to describe the dynamics of the air film by low Reynolds (Stokes flow) lubrication theory, see Appendix A for a general description. Interestingly, the Reynolds number of the drop is at lowest  $\sim 10$  and will be in general much higher, which implies that inertia dominates viscous effects in the liquid. The fact that the drop dynamics are dominated by inertia and the air film dynamics by viscosity allows us to describe our results with the Stokes number, since this dimensionless group compares inertia of the fluid to viscosity in the air film. For drops with a low impact velocity, the effect of surface tension becomes present, and the Capillary number is a relevant

dimensionless group. However, to be able to compare results more easily, the Stokes number will in general be used to describe the results. In the final stage of impact the dimple can be characterized by a dimple height  $H_d$  and an entrapped bubble volume  $V_b$ . This has been recently done by Bouwhuis et al. [9] and the result is depicted in Fig. 2.3

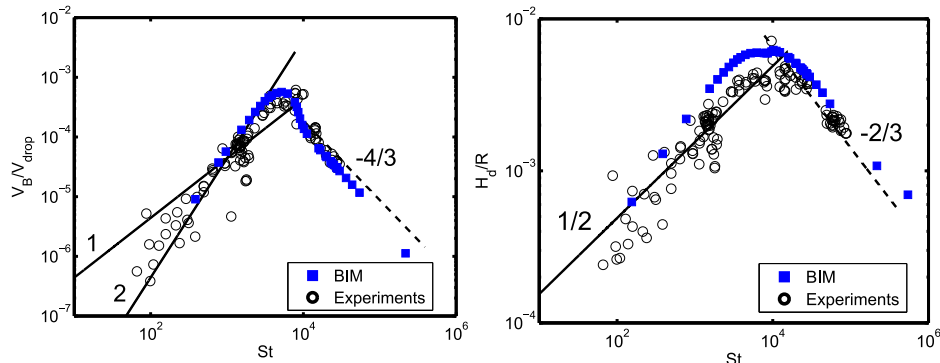


Figure 2.3: Adapted from Bouwhuis et al. [9]. Blue symbols correspond to BIM results, black open circles correspond to experimental data. The normalized bubble volume  $V_b/V_{drop}$  and normalized dimple height  $H_d/R$  exhibit a maximum which separates the two regimes governing air bubble entrainment: the inertial regime and the capillary regime. Theoretical scaling laws describing these regimes have been derived, and are also shown in this plot and are explained in the text.

As can be seen in this figure both experiments and numerics show an optimum in  $H_d$  and  $V_b$ , which is supported by theoretical scaling laws. It turns out that the optimum separates two regimes. For low impact velocities, i.e. low  $St$  the dimple formation is limited by the force of the Laplace pressure, which tries to keep the drop spherical, against the lubrication pressure in the gas, which tries to form a dimple. This regime is called the capillary regime, and the following theoretical scalings have been derived [9]:

$$H_d/R \sim St^{1/2} \quad (2.1)$$

$$V_b/V_{drop} \sim St. \quad (2.2)$$

In the case of high  $U$  it is however the inertia of the drop that reduces  $V_b$ , because the fluid needs to be slowed down by the lubrication pressure at the bottom of the drop to form a dimple which gets more difficult for drops with more inertia. This regime is called the inertial regime, and the following theoretical scalings have been derived:

$$H_d/R \sim St^{-2/3} \quad (2.3)$$

$$V_b/V_{drop} \sim St^{-4/3}. \quad (2.4)$$

Consequently, there is a maximum in  $V_b$  and  $H_d$  between the capillary regime (surface tension dominated) and the inertial regime, which is now also theoretically explained, see Bouwhuis et al. [9] for details. However, in Fig. 2.3b one can observe that experiments and BIM do not perfectly follow the  $V_b/V_{drop} \sim St$  trend in the capillary regime, but suggest a larger slope of 2. In Appendix B this is explored in greater detail: preliminary results of a Stokes-Reynolds-Young-Laplace (SRYL) model to better understand the capillary regime are presented, which doesn't take into account the inertia of the fluid which is always present to some amount in BIM.

## 2.3 Impact onto a pool

The impact of a liquid drop onto a pool of the same liquid and the impact of rigid sphere onto a liquid pool can be described with the same dimensionless numbers. In fact, the initial geometry of the problems is identical, and the difference is the deformability of the object, which is zero in case of a solid. As is explained, the air layer is characterized by a low Reynolds number, and can be described by viscous

lubrication theory, which is explained in Chapter 3.3. For the liquid, we have however a large Reynolds number. This allows for describing the dynamics of the liquid with potential flow, i.e. neglecting viscous effects. The potential problem can be solved using the Boundary Integral Method (BIM), see Cheng et al. [11] for a historical review article. BIM for potential flow will be described in Chapter 3. In Fig. 2.4 an illustration of the problem, in this case impact of a drop onto a pool, together with the used methods is shown. As is also clear from this figure, the coupling between the dynamics of the air layer and the dynamics of the liquid is essential. This coupling will be further discussed in Chapter 3.4.

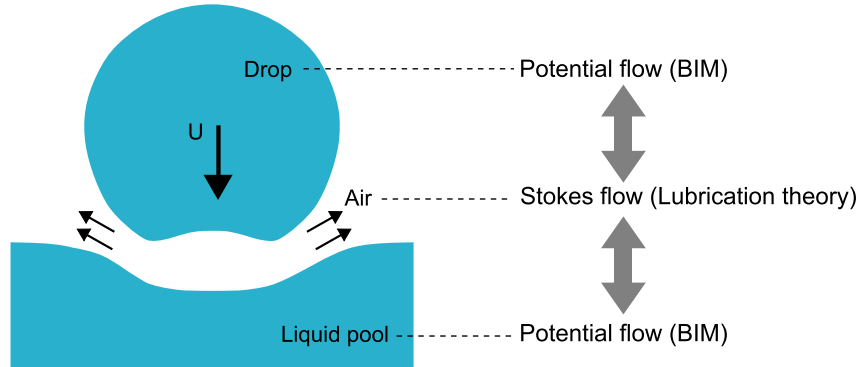


Figure 2.4: Schematic of drop impact onto a pool. For solving the dynamics, we assume potential flow in both the liquid domains. The air layer is described with Stokes flow. The gray arrows indicate that the flow of air film is coupled to the dynamics of the liquid domains and vice versa.

# Chapter 3

## Theory

In this chapter the Boundary Integral Method (BIM) for potential flow will be discussed. First the concept of potential flow will be explained. Subsequently, the BIM for solving the potential problem will be presented. The Physics of Fluid group in Twente developed a code that solves the Boundary Integral equation numerically [12]. For the case of drop impact onto a liquid pool, two distinct liquid domains were created in the original BIM code, which was originally designed for one domain. In section 3.3 lubrication theory will be developed to describe the dynamics of the air film.

### 3.1 Boundary Integral Method for Potential flow

When a flow field  $\mathbf{u}$  has a high Reynolds number, the viscous term in the Navier-Stokes equation can be neglected, and under additional assumptions [13], which are applicable for the flows we consider in this thesis, we can conclude that the flow is irrotational, i.e.  $\nabla \times \mathbf{u} = 0$ . This allows for setting up a scalar potential  $\phi$  describing the flow field:

$$\mathbf{u} = \nabla \phi \quad (3.1)$$

If in addition the Mach number  $Ma \ll 1$ , which is the case for our flows, we can conclude that the flow is incompressible. From the continuity equation [13] it then follows that the velocity field is divergence free:

$$\nabla \cdot \mathbf{u} = 0. \quad (3.2)$$

If we now substitute Eq.3.1 into Eq.3.2, we find that the velocity field  $\mathbf{u}$  obeys the Laplace equation:

$$\nabla^2 \phi = 0. \quad (3.3)$$

The fact that the velocity field obeys the Laplace equation is used to efficiently solve the potential problem, and thus the dynamics of the fluid, using the Boundary Integral Method, which is described in the next section. For setting up the boundary integral equation (BI equation) use of the free space Green's function is made. The corresponding free space Green's function  $G(\mathbf{x}, \mathbf{x}_0)$  to Eq. 3.3 has to satisfy  $\nabla^2 G(\mathbf{x}, \mathbf{x}_0) + \delta(\mathbf{x} - \mathbf{x}_0) = 0$ . The solution to this equation is given by:

$$G(\mathbf{x}, \mathbf{x}_0) = \frac{1}{4\pi|\mathbf{x} - \mathbf{x}_0|}. \quad (3.4)$$

Combining these properties of Green's function with the property of  $\phi$  being a harmonic function, Green's second identity can be used to derive the Boundary Integral equation for the solution of the potential *inside* a singly connected domain  $\phi$  [14]:

$$\phi(\mathbf{x}_0) = \int_S \frac{\partial G(\mathbf{x}, \mathbf{x}_0)}{\partial n} \phi(\mathbf{x}) dS(\mathbf{x}) - \int_S G(\mathbf{x}, \mathbf{x}_0) \frac{\partial \phi(\mathbf{x})}{\partial n} dS(\mathbf{x}) \quad (3.5)$$

The power of the Boundary Integral equation Eq. 3.5 now becomes evident: the potential  $\phi(\mathbf{x}_0)$  inside the domain is represented as a function of boundary integrals of values on the surface, hence the name Boundary Integral Method, see Fig. 3.1. This means that a 3d potential problem can be solved by solving the BI equation at the 2d surface enclosing the volume. Likewise, a 2d potential problem can be converted

to a 1d problem, where the BI equation now has to be solved for the line enclosing the surface. Thus, a substantial computational gain is obtained, because BIM lowers the dimension of the problem by one [15].

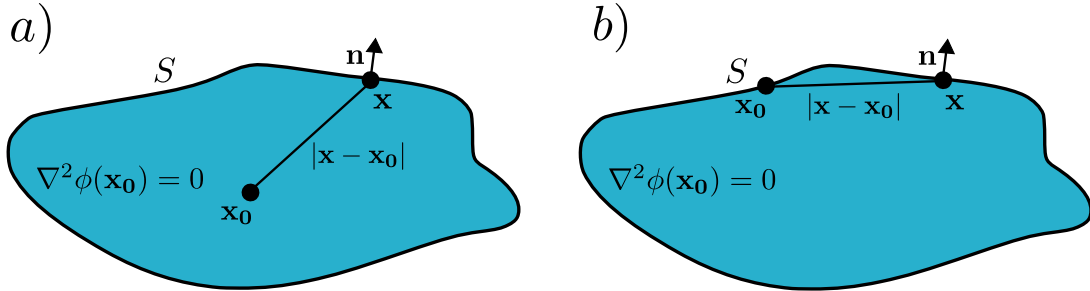


Figure 3.1: Adapted from Klaseboer et al. [15] a) Schematic of a 3d flow domain with  $\mathbf{x}_0$  located inside the domain. b) Here  $\mathbf{x}_0$  is located on the surface of the domain.  $\mathbf{n}$  is the unit normal vector.

The BI equation can be solved by putting  $\mathbf{x}_0$  on the surface, see figure Fig. 3.1b. In the case that  $\mathbf{x}_0$  is located at the surface  $S$ , the LHS of the BI equation Eq. 3.5 is slightly modified [15] and reads:

$$c\phi(\mathbf{x}_0) = \int_S \frac{\partial G(\mathbf{x}, \mathbf{x}_0)}{\partial n} \phi(\mathbf{x}) dS(\mathbf{x}) - \int_S G(\mathbf{x}, \mathbf{x}_0) \frac{\partial \phi(\mathbf{x})}{\partial n} dS(\mathbf{x}) \quad (3.6)$$

Now the potential  $\phi(\mathbf{x}_0)$  on the LHS of Eq. 3.6 is multiplied by a value  $c$ , which depends on the smoothness of the interface. It turns out that if the curvature of the interface is well-defined,  $c$  has a constant value of  $c = 1/2$ . If the interface has sharp edges with no well-defined curvature, as for example in the case where a fluid touches a solid and forms a contact line,  $c$  will not be constant. However, the problems considered in this thesis always deal with smooth fluid interfaces, so  $c$  always has the value of  $1/2$ . Since Green's function  $G(\mathbf{x}, \mathbf{x}_0)$  (and its normal derivative) is fully given, we inspect that Eq. 3.6 describes a relation between  $\phi$  and  $\frac{\partial \phi}{\partial n}$  at the surface  $S$ . We note that  $\frac{\partial \phi}{\partial n} = \mathbf{u}_n$  is the normal component of the velocity at the surface. One of these two variables  $\phi$  or  $\frac{\partial \phi}{\partial n}$  has to be known in order to solve for the remaining unknown variable. This depends on type of boundary condition at the surface, as will be explained in the next section.

## 3.2 Boundary conditions

The type of boundary at the fluid surface determines what kind of boundary condition is employed. Two cases can be distinguished. Either the fluid surface is a free surface, or the fluid is touching a solid and we deal with a solid boundary.

If the fluid is touching a solid wall at some point, the normal velocity  $\frac{\partial \phi}{\partial n}$  of the fluid is specified by the velocity of that solid wall, since the fluid has to move along with the wall. The boundary condition for the potential at a solid wall will thus be a Neumann boundary condition  $\frac{\partial \phi}{\partial n} = -U_{wall}$ . Here the  $U_{wall}$  is the normal velocity of the wall, which is simply zero if we deal with a rigid wall. While  $\frac{\partial \phi}{\partial n}$  is specified at the solid boundary, the potential  $\phi$  itself will be unknown.

If the fluid surface is a free surface instead of a solid boundary,  $\frac{\partial \phi}{\partial n}$  will be unknown. However,  $\phi$  at the free surface can be found using the unsteady Bernoulli equation which has to be valid at the free surface [13]:

$$\frac{\partial \phi}{\partial \tau} = -\frac{1}{2} |\nabla \phi|^2 - \mathbf{g} \cdot \mathbf{x}_0 - \frac{\gamma \kappa(r, \tau) + p}{\rho_l} \quad (3.7)$$

Here  $\gamma$  is the interfacial tension,  $\kappa$  is the local curvature of the interface,  $\mathbf{g}$  is the acceleration of gravity,  $\tau$  is time, and  $p$  is the pressure at the exterior of the drop. Given a certain initial condition  $\phi_0(r, \tau_0)$  one can find  $\phi(r, \tau > \tau_0)$  by integrating in time. In practice, this is done numerically: each time step the new potential  $\phi(r, \tau > \tau_0)$  has to be found by integrating the given  $\phi_0(r, \tau_0)$  of the current timestep.

Furthermore, the free interface has to move with the local velocity, which is known as the kinematic boundary condition. This effectively means that there can be now fluid flow across the interface which means that a fluid particle  $\mathbf{x}_s$  at the surface will be displaced according to the local velocity:

$$\frac{D\mathbf{x}_s}{D\tau} = \nabla\phi. \quad (3.8)$$

Summarizing, we conclude that the BI equation 3.6 can be solved by providing either  $\phi$  or  $\frac{\partial\phi}{\partial n}$  at the surface using the appropriate boundary condition. In this thesis we only deal with free fluid surfaces which means that  $\phi$  will be known at the surface, and Eq. 3.6 can be used to solve for  $\frac{\partial\phi}{\partial n}$ . For a more detailed numerical implementation the reader will be referred to [16].

### 3.3 Lubrication approximation for Stokes flow

In this section lubrication theory for drop impact onto a solid surface will be developed and extended to the case of drop impact onto a liquid pool, which demands a more careful approach since we now deal with a deformable subphase instead of a undeformable flat solid surface. For impact of a rigid sphere onto a pool, we can use the same lubrication equations as for drop impact onto a pool.

#### 3.3.1 Drop impact onto a flat surface

A definition sketch of drop impact onto a solid surface is depicted in Fig. 3.2. The air which needs to be squeezed out when the drop is approaching the solid surface is essential for the dynamics of the drop. Due to an increase in air pressure right under the impacting drop, the interface will deform locally: a dimple is formed before the drop touches the surface. The dynamics of the thin air film trapped between the impacting drop and the solid surface is characterized by a thin film Reynolds number  $Re_g = \rho U h_d / \mu$ , as is described in Chapter 2. Here  $U$  is the impact velocity of the drop and  $h(r, t)$  is the film thickness. Furthermore,  $\rho$  is the density of air and  $\mu$  is the dynamic viscosity of air.

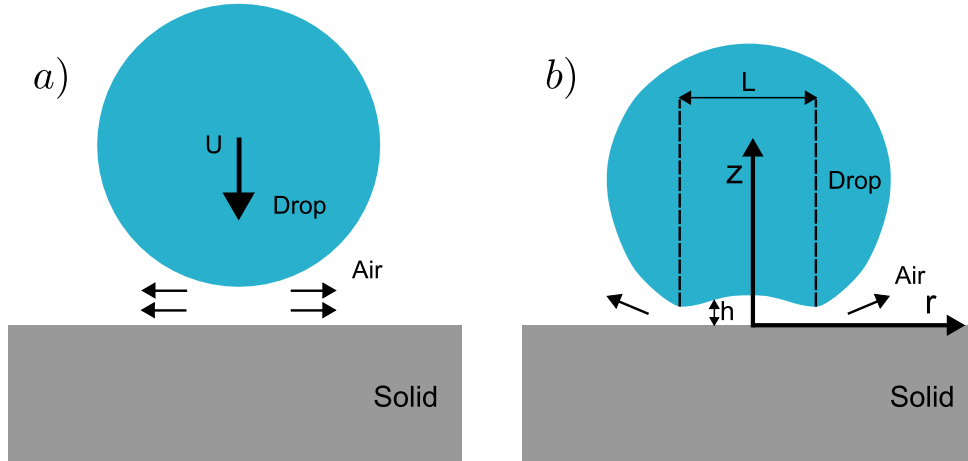


Figure 3.2: a) Schematic of drop impact on a solid surface. Air needs to be squeezed out when the drop is approaching the surface. b) Due to the increase of air pressure a dimple is formed before the drop touches the surface. The air film which is trapped between the drop and the surface is characterized by a thickness  $h(r, t)$  and a lateral extension  $L$ .

The highest Reynolds number in the explored parameter range is  $Re \sim 0.1$  and we can use lubrication theory as described in Appendix A. In that case the Navier-Stokes equations can be written as:

$$\frac{\partial p}{\partial r} = \mu \frac{\partial^2 u_r}{\partial z^2}. \quad (3.9)$$

We can integrate equation Eq. 3.9 twice with respect to  $z$ , employing a no slip boundary condition at the solid surface ( $u_r = 0$  at  $z = 0$ ) as well as at the surface of the drop ( $u_r = U_d(r, t)$  at  $z = h$ ):

$$u_r = U_d \left( \frac{z}{h} \right) + \frac{1}{2\mu} \frac{\partial p}{\partial r} (z^2 - zh). \quad (3.10)$$

The first term of Eq 3.10 can be associated with Couette flow, caused by the movement of the drop surface. The second term can be associated with Poiseuille flow, which is driven by the radial pressure gradient [17]. Assuming that the air flow is incompressible ( $Ma \ll 1$ ), mass conservation is given by:

$$\int_0^h \frac{1}{r} u_r dz + \frac{\partial}{\partial r} \int_0^h u_r dz + \dot{h} = 0. \quad (3.11)$$

Here the fact that the surface of the interface moves with the local velocity is used, which is known as the kinematic boundary condition:

$$\left. \frac{\partial h}{\partial t} \right|_{z=h} + \frac{\partial h}{\partial r} u_r|_{z=h} - u_z|_{z=h} = 0 \quad (3.12)$$

We now substitute our expression for  $u_r$  in Eq. 3.11:

$$\int_0^h \frac{1}{r} \left[ U_d \left( \frac{z}{h} \right) + \frac{1}{2\mu} \frac{\partial p}{\partial r} (z^2 - zh) \right] dz + \frac{\partial}{\partial r} \left( \int_0^h \left[ U_d \left( \frac{z}{h} \right) + \frac{1}{2\mu} \frac{\partial p}{\partial r} (z^2 - zh) \right] dz \right) + \dot{h} = 0. \quad (3.13)$$

Performing the integration and multiplying with  $r$ , we find:

$$\left[ U_d \frac{h}{2} - \frac{h^3}{12\mu} \frac{\partial p}{\partial r} \right] + r \frac{\partial}{\partial r} \left( \left[ U_d \frac{h}{2} - \frac{h^3}{12\mu} \frac{\partial p}{\partial r} \right] \right) + r \dot{h} = 0. \quad (3.14)$$

We can now combine the first two terms of the LHS, which is essential in solving for  $\frac{\partial p}{\partial r}$ :

$$\frac{\partial}{\partial r} \left( r \left[ U_d \frac{h}{2} - \frac{h^3}{12\mu} \frac{\partial p}{\partial r} \right] \right) + r \dot{h} = 0. \quad (3.15)$$

We now can write Eq. 3.15 like:

$$r U_d \frac{h}{2} - \frac{r h^3}{12\mu} \frac{\partial p}{\partial r} = \int_0^r -\tilde{r} \dot{h} d\tilde{r}. \quad (3.16)$$

Solving for  $\frac{\partial p}{\partial r}$  gives an expression which we can integrate numerically to compute the pressure  $p$  in the film:

$$\frac{\partial p}{\partial r} = \frac{12\mu}{r h^3} \int_0^r \tilde{r} \dot{h} d\tilde{r} + \frac{6\mu U_d}{h^2}. \quad (3.17)$$

The second term of the RHS is the extra term due to movement of the drop surface in the radial direction.

### 3.3.2 Drop impact on a liquid pool

The lubrication equations for impact on a pool will be derived in several steps. The approach will be the same as for drop impact onto a flat surface, but we will see that the geometry of the thin air film will be different, since the pool, just like the drop, will also deform. This will result in slightly more complicated equations.

#### Mass conservation

We start with continuity in cylindrical coordinates:

$$\frac{u_r}{r} + \frac{\partial u_r}{\partial r} + \frac{\partial u_z}{\partial z} = 0. \quad (3.18)$$

A definition sketch of drop impact on a liquid pool is depicted in Fig. 3.3. Here the drop surface is taken as a reference, and the curvilinear coordinate  $t$  is defined along the drop, starting at the center of symmetry. At some large radial coordinate where  $t = T$  we assume atmospheric pressure. The coordinate perpendicular to  $t$  is defined to be  $n$ . The gap height  $h$  is defined as the length of the perpendicular line from the drop projected onto the liquid pool. The two surfaces are assumed to be nearly parallel ( $|\partial_t h| \ll 1$ ), so we can apply lubrication theory.

It can be shown that for this new  $(t, n)$ -coordinate system, the continuity equation can be written as [16]:

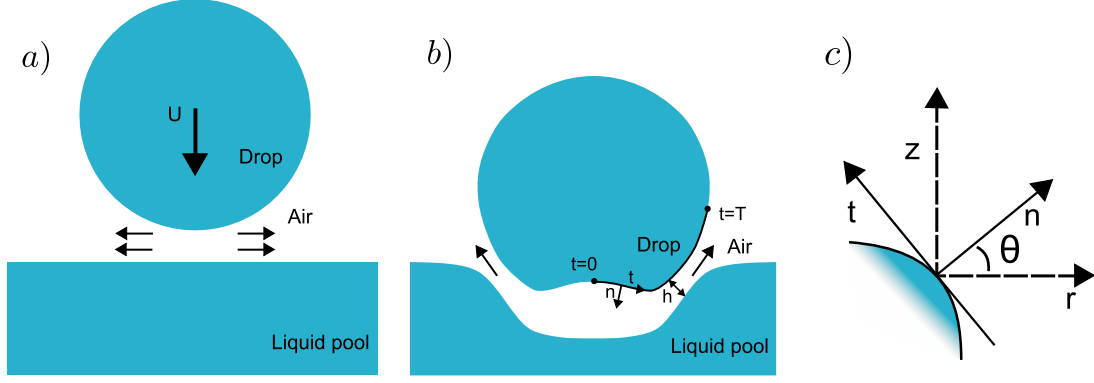


Figure 3.3: a) Schematic of drop impact on a liquid pool. b) Definition of the curvilinear  $(t,n)$ -coordinate system.

$$\frac{u_r}{r} + \frac{\partial u_t}{\partial t} + \frac{\partial u_n}{\partial n} = 0. \quad (3.19)$$

At the interface of the liquid pool ( $n = h$ ) we know that the fluid particles have to move with the interface. This is mathematically described with the kinematic boundary condition:

$$\dot{h} + \left( u_t \frac{\partial h}{\partial t} \right) \Big|_{n=h} = u_n|_{n=h} - u_n|_{n=0}. \quad (3.20)$$

Here  $\dot{h}$  is the time derivative of  $h$ . We emphasize that  $t$  is the curvilinear coordinate and not time. We now integrate Eq. 3.19 along  $h$  and obtain:

$$\int_0^h \frac{u_r}{r} dn + \int_0^h \frac{\partial u_t}{\partial t} dn = - \int_0^h \frac{\partial u_n}{\partial n} dn = u_n|_{n=0} - u_n|_{n=h}. \quad (3.21)$$

Using Leibniz integral rule for the second integral we find:

$$\int_0^h \frac{u_r}{r} dn + \frac{\partial}{\partial t} \int_0^h u_t dn - \left( u_t \frac{\partial h}{\partial t} \right) \Big|_{n=h} = u_n|_{n=0} - u_n|_{n=h}. \quad (3.22)$$

We now use the kinematic boundary condition formulated in Eq. 3.20 for the third term on the LHS to obtain:

$$\int_0^h \frac{u_r}{r} dn + \frac{\partial}{\partial t} \int_0^h u_t dn + \dot{h} - u_n|_{n=h} + u_n|_{n=0} = u_n|_{n=0} - u_n|_{n=h}. \quad (3.23)$$

Canceling the terms  $u_n|_{n=h}$  and  $u_n|_{n=0}$  on both sides gives:

$$\int_0^h \frac{u_r}{r} dn + \frac{\partial}{\partial t} \int_0^h u_t dn + \dot{h} = 0. \quad (3.24)$$

We still have to describe  $u_r$  within the new  $(t,n)$ -coordinate system. Therefor we substitute  $u_r = u_n \cos(\theta) - u_t \sin(\theta)$  in the equation above to get:

$$\int_0^h \frac{1}{r} u_n \cos(\theta) dn - \int_0^h \frac{1}{r} u_t \sin(\theta) dn + \frac{\partial}{\partial t} \int_0^h u_t dn + \dot{h} = 0. \quad (3.25)$$

We assumed in lubrication theory that  $u_n$  is small, so we neglect the first term. The second term is an integral with respect to  $n$  containing the variable  $r$ . This radial coordinate  $r$  across  $h$  is a function of  $n$ :  $r = n \cos \theta + c(t)$ . Here  $c = c(t)$  is the value of  $r$  at the drop surface ( $n = 0$ ) for some coordinate  $t$ . We thus substitute this expression for  $r$  into Eq 3.25 and neglect the first term to find:

$$- \int_0^h \frac{\sin(\theta)}{n \cos \theta + c} u_t dn + \frac{\partial}{\partial t} \int_0^h u_t dn + \dot{h} = 0. \quad (3.26)$$

### Flow profile within the air film

Just like the case of drop impact onto a flat surface, we assume a small thin film Reynolds number  $Re \ll 1$ . Again, the geometry of the problem allows us to use lubrication theory. In the case of impact on a pool, the Navier-Stokes equations can then be written as:

$$\frac{\partial p}{\partial t} = \mu \frac{\partial^2 u_t}{\partial n^2}. \quad (3.27)$$

We can integrate equation Eq. 3.27 twice with respect to  $n$ , employing a no slip boundary condition at the drop surface ( $u_t = U_d$  at  $n = 0$ ) as well as at the surface of the pool ( $u_t = U_b$  at  $n = h$ ):

$$u_t = \left( (U_b - U_d) \frac{n}{h} + U_d \right) + \frac{1}{2\mu} \frac{\partial p}{\partial t} (n^2 - nh). \quad (3.28)$$

The first term of Eq. 3.28 can be associated with Couette flow, caused by the movement of interfaces. The second term can be associated with Poiseuille flow, which is driven by the radial pressure gradient [17]. Substituting this expression for  $u_t$  in our equation for mass conservation, Eq. 3.26, we get:

$$\begin{aligned} & - \int_0^h \frac{\sin(\theta)}{n \cos \theta + c} \left[ \left( (U_b - U_d) \frac{n}{h} + U_d \right) + \frac{1}{2\mu} \frac{\partial p}{\partial t} (n^2 - nh) \right] dn \\ & + \frac{\partial}{\partial t} \int_0^h \left[ \left( (U_b - U_d) \frac{n}{h} + U_d \right) + \frac{1}{2\mu} \frac{\partial p}{\partial t} (n^2 - nh) \right] dn + \dot{h} = 0. \end{aligned} \quad (3.29)$$

In the first integral we deal with a prefactor  $\sin(\theta)/(n \cos \theta + c)$ . When taking into account the geometry of the problem into account we note that  $n \cos \theta \ll c$ . We thus assume  $\sin(\theta)/(n \cos \theta + c) \approx \sin(\theta)/c$ . Performing the integrals of Eq. 3.29 under this assumption yields:

$$-\frac{\sin(\theta)}{c} \left( \frac{h}{2} (U_b + U_d) - \frac{h^3}{12\mu} \frac{\partial p}{\partial t} \right) + \frac{\partial}{\partial t} \left( \frac{h}{2} (U_b + U_d) - \frac{h^3}{12\mu} \frac{\partial p}{\partial t} \right) + \dot{h} = 0. \quad (3.30)$$

We note that one cannot combine the first two terms of the LHS of the equation above easily, unlike the case of impact on a flat plate, where we could nicely combine the two terms, as was done in going from Eq. 3.14 to Eq. 3.15. We now have to work a bit harder to obtain an expression for  $\frac{\partial p}{\partial t}$ . If we adopt  $G(t) = \left( \frac{h}{2} (U_b + U_d) - \frac{h^3}{12\mu} \frac{\partial p}{\partial t} \right)$  we can transform the equation above to a first order inhomogeneous linear ODE for  $G(t)$ :

$$\dot{G}(t) - a(t)G(t) = f(t). \quad (3.31)$$

Here  $a(t)$  and  $f(t)$  are known functions of  $t$ :

$$a(t) = \frac{\sin(\theta)}{c} \quad (3.32)$$

$$f(t) = -\dot{h} \quad (3.33)$$

### Solving first order inhomogeneous ODE

To solve Eq. 3.31 we define an integrating factor  $\tilde{I}(t) = e^{-\int a(t)dt} = e^c e^{-\int_0^t a(\tilde{t})d\tilde{t}}$ . Here  $e^c$  is an integration constant. We multiply both sides of Eq. 3.31 with the integrating factor  $\tilde{I}(t)$  to obtain:

$$(\tilde{I}G)' = \tilde{I}(\dot{G} - aG) = \tilde{I}f \quad (3.34)$$

Integrating this equation yields:

$$I(t)G(t) = \int_0^t I(\tilde{t})f(\tilde{t})d\tilde{t} + K \quad (3.35)$$

Here we have defined  $I(t) = e^{-\int_0^t a(\tilde{t})d\tilde{t}}$  and absorbed  $e^c$  in the integration constant  $K$ . Solving for  $G(t)$  finally gives us:

$$G(t) = \frac{1}{I(t)} \left( \int_0^t I(\tilde{t})f(\tilde{t})d\tilde{t} + K \right) \quad (3.36)$$

The integration constant  $K$  should be taken such that  $G(t) = 0$  for  $t = 0$ , because we have zero pressure gradient in the center of symmetry, and also zero tangential velocities. Because the integral  $\int_0^t I(\tilde{t})f(\tilde{t}) d\tilde{t}$  goes to zero for  $t = 0$ , we conclude  $K = 0$ .

We can now substitute  $G(t) = \left(\frac{h}{2}(U_b + U_d) - \frac{h^3}{12\mu} \frac{\partial p}{\partial t}\right)$  to write an equation for  $\frac{\partial p}{\partial t}$ , noting that we have to evaluate two numerical integrals to calculate  $\frac{\partial p}{\partial t}$ :

$$\frac{\partial p}{\partial t} = -\frac{12\mu}{h^3} \left( \frac{1}{I(t)} \left( \int_0^t I(\tilde{t})f(\tilde{t}) d\tilde{t} \right) - \frac{h}{2} (U_b + U_d) \right) \quad (3.37)$$

with

$$I(t) = e^{-\int_0^t a(\tilde{t})d\tilde{t}}. \quad (3.38)$$

We note that for calculating  $p(t)$  we have to evaluate three numerical integrals compared to two numerical integrals in the case of impact on a flat plate. As a check of our analysis we now orientate the  $(t,n)$ -coordinate system in such away that  $t = r$ , to recover the situation for drop impact onto a flat plate. In that case we have  $\theta = -\pi/2$ , and we can write for  $a$ :

$$a(r) = \frac{\sin\theta}{r} = -\frac{1}{r} \quad (3.39)$$

The integrating factor  $I$  now becomes:

$$I(r) = e^{-\int_0^r a(\tilde{r})d\tilde{r}} = e^{\ln r} = r \quad (3.40)$$

Under the proposition  $t = r$ , which resembles the more simple coordinate system of drop impact onto a solid surface, we also have  $U_b = 0$ . We can now write Eq. 3.37 as:

$$\frac{\partial p}{\partial r} = -\frac{12\mu}{h^3} \left( \frac{1}{I(r)} \left( \int_0^r I(\tilde{r})f(\tilde{r}) d\tilde{r} \right) - \frac{h}{2} (U_b + U_d) \right) = \frac{12\mu}{h^3} \left( \frac{1}{r} \left( \int_0^r \tilde{r}\dot{h} d\tilde{r} \right) + \frac{h}{2} U_d \right) \quad (3.41)$$

We see that Eq. 3.17 derived in the previous section for drop impact onto a solid is recovered by Eq. 3.41 which was derived by taking Eq. 3.37 for  $t = r$ , which gives a consistency check for our analysis.

### 3.4 Coupling air dynamics to the BIM

The description of the air flow dynamics with lubrication theory is not enough to describe the whole impact event. As is explained in Chapter 2, a coupling is needed with the liquid that is described by potential flow solved by using BIM. This coupling is realized by using an additional pressure term  $P_g$  in the unsteady Bernoulli equation Eq. 3.7, which serves as a boundary condition in the BIM as described in Chapter 3. The unsteady Bernoulli equation with the extra term for the gas pressure  $P_g$  reads:

$$\frac{\partial\phi}{\partial\tau} = -\frac{1}{2}|\nabla\phi|^2 - \mathbf{g} \cdot \mathbf{x}_0 - \frac{\gamma\kappa(r, \tau) + (P_g - P_{atm})}{\rho_l} \quad (3.42)$$

In Fig. 3.4 an illustration of the numerical implementation is shown. The air pressure  $P_g$  is calculated using the lubrication equations as described in the previous sections 3.3.1 and 3.3.2.  $P_g$  serves as an input for solving the BI equation Eq. 3.42 for the next timestep via the unsteady Bernoulli equation. The solution of the BI equation will give the current shape evolution of both the drop and the pool. Subsequently, the lubrication pressure  $P_g$  can again be determined as function of the shape evolution and serves as a new input to solve the BI equation of the next time step. The pressure will be solved from  $r = 0$  until some large radial coordinate  $r_{max}$ , where the pressure is negligible small, which is in practice taken as  $r_{max} = 0.7R$ . Here  $R$  is the radius of the drop.

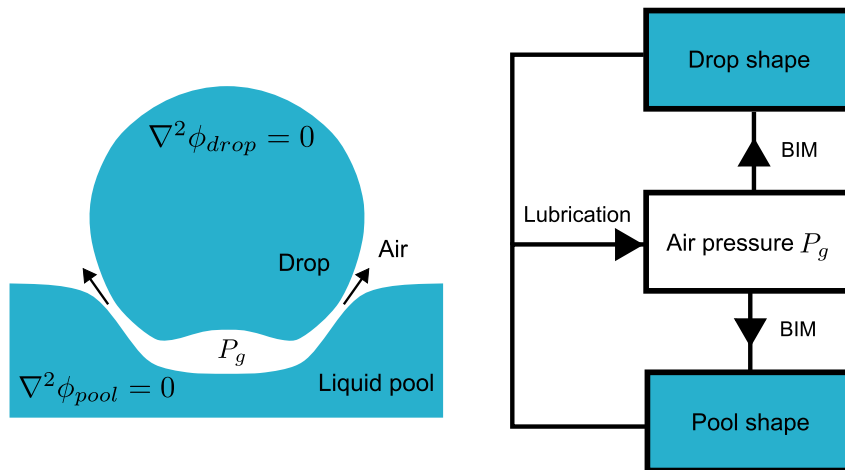


Figure 3.4: Feedback mechanism of the solving routine: The air pressure  $P_g$  is calculated and serves as input for the BIM. Subsequently, the drop and pool shape get updated, and this allows for the next calculation of  $P_g$ , and so forth.

## Chapter 4

# Air entrainment during solid sphere impact on a liquid pool

In this chapter we consider air entrainment during the impact of a rigid sphere onto a liquid pool numerically, and compare it to experimental data from Marston et al. [3]. Potential flow is used for the liquid pool and solved using BIM as described in Chapter 3 coupled to a viscous lubrication air layer as described in Chapter 3.3.2.

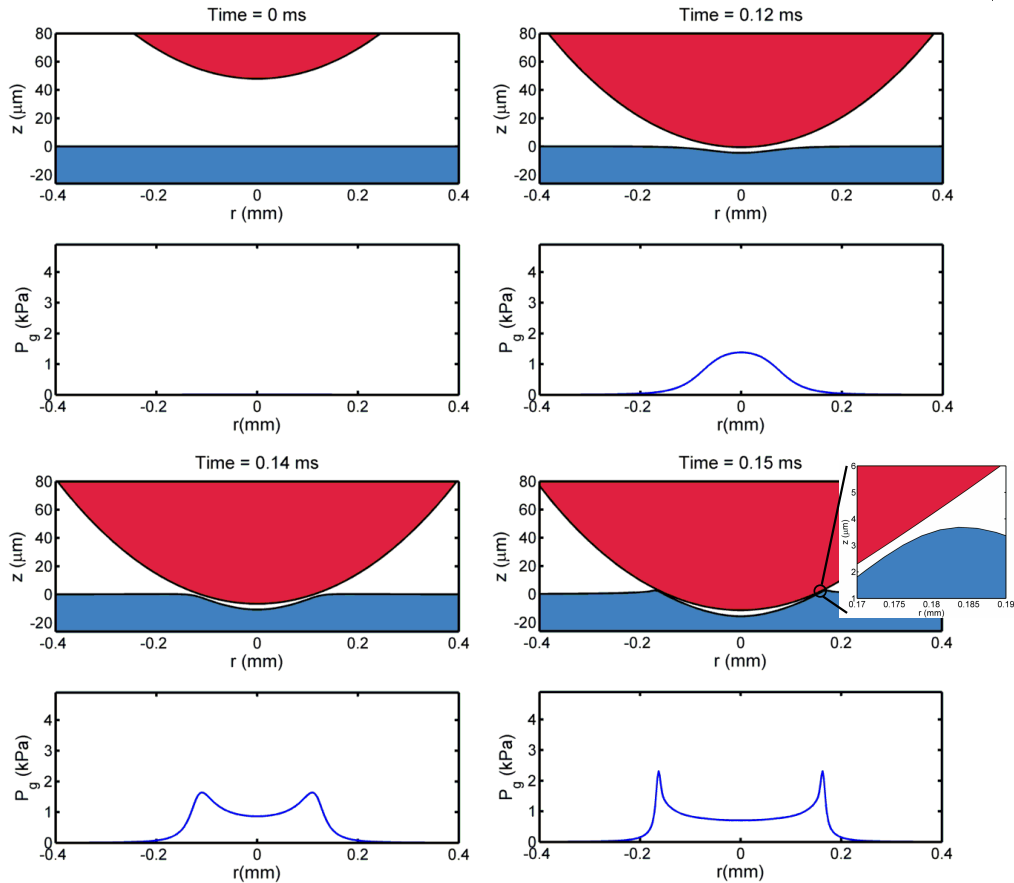


Figure 4.1: Rigid sphere impact onto a liquid pool. Note the different length scales for the  $x$ -axis and  $y$ -axis in the shape plots. The impact speed is  $U = 0.42 \text{ m/s}$  and the radius is  $R = 0.95 \text{ mm}$ . The density and surface tension of the fluid are respectively  $\rho = 916 \text{ kg/m}^3$  and  $\gamma = 0.020 \text{ N/m}$ . The simulation starts at time  $t = 0 \text{ ms}$  at an separation of  $h = 50 \mu\text{m}$ . Due to the approach of the sphere, the excess air pressure  $P_g$  will increase and acts on the liquid pool ( $t = 0.12 \text{ ms}$ ). At the final stage  $t = 0.15 \text{ ms}$  the interfaces are very close to each other ( $\sim 0.4 \mu\text{m}$ ) and the simulation is stopped.

## 4.1 Time evolution of sphere impact onto liquid pool

A typical result is depicted in Fig. 4.2. In the first frame corresponding to  $t = 0\text{ ms}$  the initial condition of the simulation is shown. In all simulations the sphere is released from an initial height of  $h_0 = 50\ \mu\text{m}$ . Convergence tests regarding the initial release height have been conducted, and releasing the sphere from a larger height gave almost the same results. The physical reason is that the lubrication pressure goes to zero for large separation of the sphere and the pool, and it turned out that  $h_0 = 50\ \mu\text{m}$  is large enough to have a negligible lubrication pressure at this height. At  $t = 0.12\text{ ms}$  the pool starts to feel the sphere, and the interface is deforming. In the lower panel of this frame, the increase in pressure is indeed visible. At  $t = 0.14\text{ ms}$  the sphere is getting closer to the pool, and the interface has been further deformed. It can also be noted that the pressure maximum is not located in the center at  $r = 0$  anymore, but now corresponds to a location where the separation between the sphere and the pool is smallest. In the final frame  $t = 0.15\text{ ms}$  we observe that the two interfaces are very close together ( $\sim 0.4\ \mu\text{m}$ ). Typically, at this point where the air gap is  $\sim 0.4\ \mu\text{m}$ , the pressure  $P_g$  will diverge and we cannot continue simulation. Though, we do note that the interfaces up to this final stage are very well resolved, which is shown in the inset in the final frame in Fig. 4.1. We further note from the final frame that an microscopic air film finds itself trapped between the sphere and the pool. It is this entrapped air that constitutes the air bubble that is dragged into the liquid, as will be further discussed in the next section.

## 4.2 Contact diameter at impact

Marston et al. [3] performed experiments of steel spheres impacting on various liquid pools and studied the air bubble that is formed at the bottom of the sphere. A high-speed image sequence of the air bubble entrainment that they captured is shown in Fig. 4.2a. A contact diameter  $D_c$  is defined as the diameter of initial contact of the sphere with the pool. As is shown in Fig. 4.2a, this already happens in the second frame. It has been reasoned by Marston et al. [3] that this initial contact diameter  $D_c$  sets the bubble volume, because after contact the air sheet merely contracts to form a hemispherical air bubble, but the total volume of air that is entrapped is already determined. Since our simulations do not capture the complex dynamics after contact (which involves a moving contact line), it will be insightful to compare our numerical value for the initial contact diameter  $D_c$ , which is taken as the peak-to-peak distance of the two local maxima of the liquid pool, see Fig. 4.2b. These maxima are close to the location of the minimum air gap and are thought to represent the detection of the diameter in experiment best. The experimental results for  $D_c$  from Marston et al. [3] together with the BIM results are shown in Fig. 4.3. We see that the BIM results, which are shown as red solid circles, are in reasonable agreement with the trend that is shown by the experimental data. Though we cannot simulate the subsequent collapse of the air film into a bubble, the agreement in  $D_c$  suggests that we will be able to estimate the total bubble volume  $V_b$  which is enclosed by the two interfaces.

## 4.3 Entrapped air bubble volume

The air bubble volume  $V_b$  is determined at the final stage of impact as shown in Fig. 4.2c by numerically integrating the trapped air film starting from the location of minimum separation. The result of  $V_b$  versus  $St$  is depicted in Fig. 4.4a, where the Stokes number  $St$  is varied by varying the impact velocity only. We find excellent agreement with experimental data. Also, the BIM results (yellow triangles) agree with the theoretical description  $V_b/V \sim St^{-4/3}$  (solid line), which has been successfully developed to describe bubble entrainment during drop impact onto a flat surface [18, 19, 9], see also Chapter 2. It seems that there is a similar mechanism for bubble entrainment during impact of a solid sphere onto a pool and liquid drop impact onto a solid, which has also been suggested by Marston et al. [3]. The apparent universal mechanism for bubble entrainment will be further discussed in Chapter 5.1.

For calculating  $V_b$  the final frame as depicted in Fig. 4.2c is considered where the minimum air gap thickness  $h_{min} = 0.4\ \mu\text{m}$ . It is required that the air bubble volume has been converged at this stage. To check this assumption, the bubble volume has been also determined at  $h_{min} > 0.4\ \mu\text{m}$ . This result is shown in Fig. 4.4b. We conclude that  $V_b$  is determined accurately, although we were not able to simulate until  $h_{min} = 0\ \mu\text{m}$ , because  $h_{min} = 0.6\ \mu\text{m}$  gives similar results.

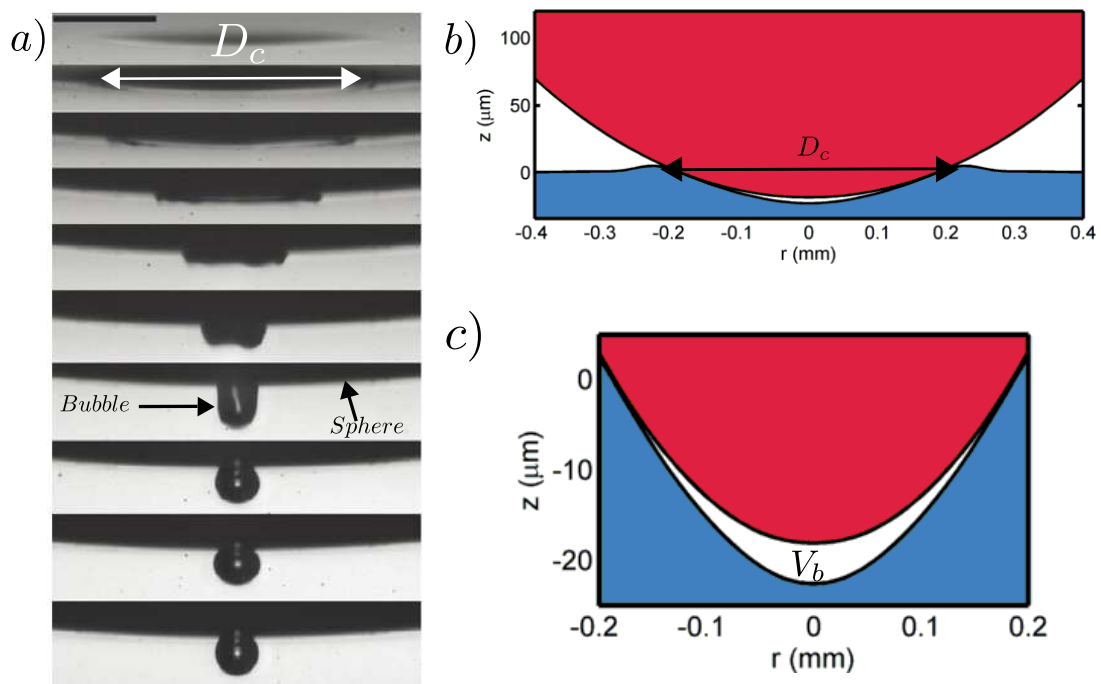


Figure 4.2: a) High-speed image sequence taken and modified from Marston et. al [3]. The scale bar represents  $500 \mu\text{m}$  b) Numerical determination of  $D_c$  c) Same snapshot as in b, zoomed in on the air film to indicate the entrapped bubble volume  $V_b$ .

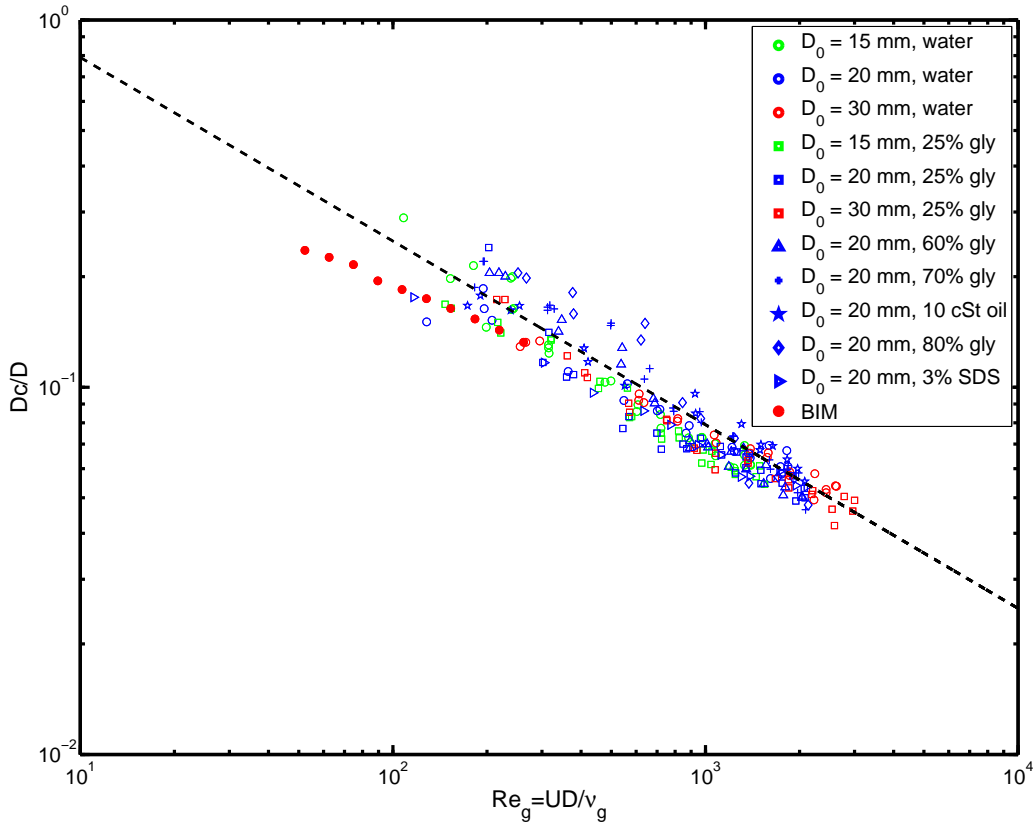


Figure 4.3: Experimental data for the contact diameter  $D_c$  normalized by the sphere diameter  $D$ , taken from Marston et. al [3] who are acknowledged for providing their original data set. A general trend independent of viscosity has been found for various spheres of diameter  $D$ . BIM results are in reasonable agreement with this trend.

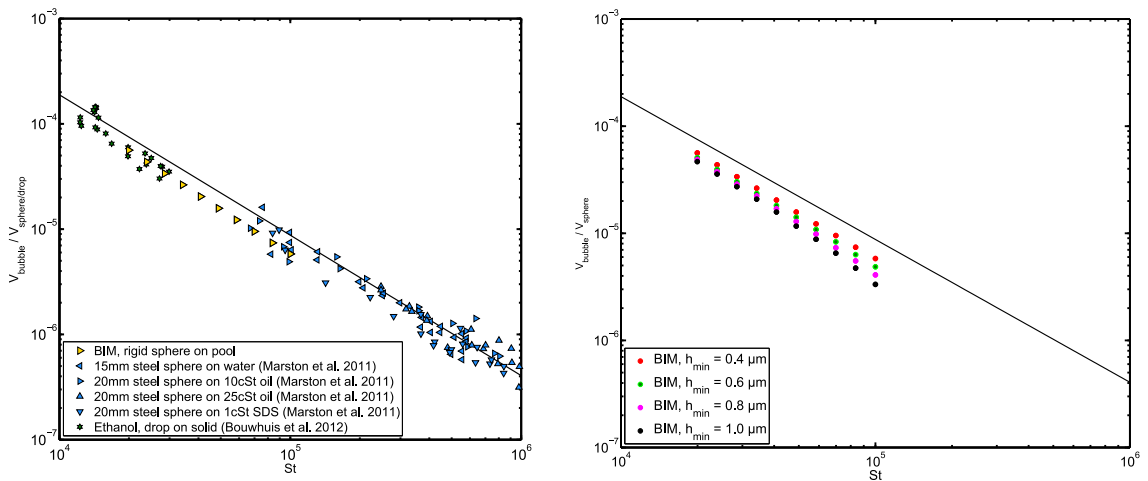


Figure 4.4: a) Normalized bubble volume versus Stokes number. BIM gives good agreement with various experiments and the theoretical slope of  $-4/3$ . b) BIM results for different  $h_{min}$ . This indicates that further decreasing  $h_{min}$  is not expected to affect the final bubble volume  $V_b$  much.

## Chapter 5

# Drop impact onto a liquid pool

Drop impact onto a liquid pool is different compared to impact of a rigid sphere onto a pool because the impacting object, the drop, is a deformable object. This means that the pressure build up in the air layer will affect both the liquid pool and the drop. In this Chapter drop impact onto a pool and the subsequent air entrapment is discussed. A numerical result is depicted in Fig 5.1. As is clear from this figure, both the drop and the pool deform, unlike rigid sphere impact on a pool which is depicted the previous chapter, Fig. 4.1. Just like is described in Chapter 4, a bubble will be entrapped due to the deformation of the interfaces, which will be investigated in detail below.

### 5.1 Entrapped air bubble volume

Similar as was done in Chapter 4 the bubble volume  $V_b$  is determined in the final stage of impact, where the air gap thickness  $h_{min} = 0.4 \mu m$ . This numerical bubble volume will be compared to recent experimental data [6], see Fig. 5.3. In this figure we see a drop entering a liquid pool when looking from the side. In the first three frames we observe a stable air film between the drop and the pool. In the subsequent frame at  $0 ms$  we observe rupture of the air film, because the interfaces are so close to each other at this point that they will touch, i.e they coalesce. After coalescence surface tension contracts the air film into an air bubble, which can be measured.

When comparing the numerics in Fig. 5.1 to the experiment Fig. 5.2 one difference can be noted: the distance the drop travels into the pool before the air film ruptures. In the case of experiment, the drop sinks deep into the pool ( $\sim mm$ ) before rupture, while in case of numerics, where rupture is assumed to occur at  $h_{min} = 0.4 \mu m$ , the drop does not penetrate the pool that much ( $\sim \mu m$ ). The penetration depth of the drop into the pool will be further discussed in Chapter 5, we will now first focus on the air bubble volume  $V_b$  that is entrapped. The numerical result for  $V_b$  (yellow circles), together with recent experimental data for drop impact onto a pool [6] (red symbols), is depicted in Fig. 5.3. We again find excellent agreement between BIM simulations and experimental data. In this figure also the data for sphere impact onto a pool (simulations shown as yellow triangles, experiment as blue triangles), and experimental data for drop impact onto a solid from Fig. 4.4 (green symbols) are shown.

As can be seen from the figure, the same scaling  $V_b \sim St^{-4/3}$  holds for drop impact onto a pool (both numerics and experiments), but there is an offset from the rest of the data for which only one of the interfaces is deformable, i.e. the case of sphere impact onto a pool, or drop impact onto a solid. Intuitively we can understand this offset: when we deal with two deformable interfaces (liquid drop and pool) both interfaces can be deformed to make more room for an air bubble compared to the case when we deal with only one deformable interface. To further investigate this, we investigate the deformation  $\delta$  of the interfaces. A definition sketch of  $\delta$  is shown in Fig. 5.4.

The time evolution of the deformation  $\delta$  of both the pool and the drop are displayed in Fig. 5.5. We note that  $\delta$  for the pool and the drop are behaving very similar, they are almost identical. In the final frame  $t = 0.13 ms$   $\delta$  of the pool for rigid sphere impact with the same velocity is superimposed. We note that  $\delta$  of the sphere impact simulation is of similar magnitude compared to  $\delta$  of the drop impact onto a pool. The fact that  $\delta$  is so similar for both interfaces, and the fact that we deal with two deformable interfaces instead of one, leads us to the suspicion that the entrapped bubble in case of drop impact onto a pool compared to sphere impact onto a pool might differ by a factor 2. This hypothesis is tested by first plotting the results from Fig. 5.3, but now we include also the BIM results that have been found in the capillary regime for drop impact onto a pool, see Fig. 5.6. These results have been initially omitted

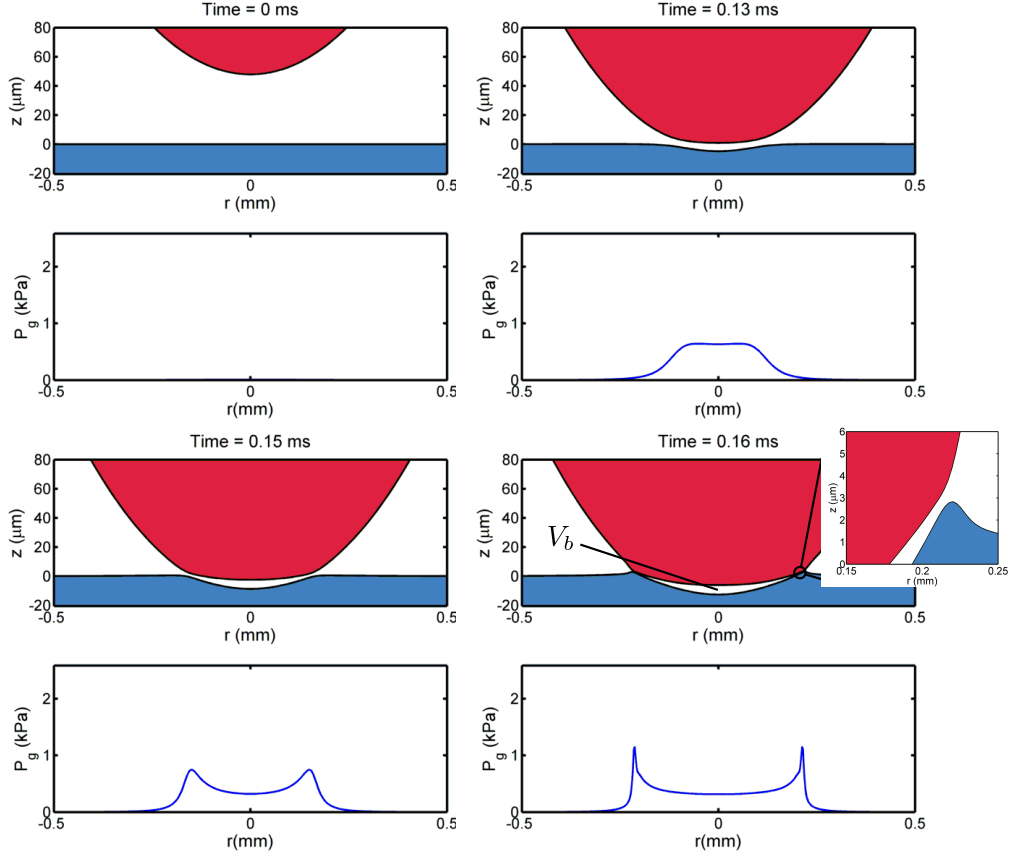


Figure 5.1: Drop impact onto a liquid pool. Note the different length scales for the  $x$ -axis and  $y$ -axis in the shape plots. The impact speed is  $U = 0.42 m/s$  and the radius is  $R = 0.95 mm$ . The density and surface tension of the fluid are respectively  $\rho = 916 kg/m^3$  and  $\gamma = 0.020 N/m$ . The simulation starts at time  $t = 0 ms$  at an separation of  $h = 50 \mu m$ . Due to the approach of the sphere, the excess air pressure  $P_g$  will increase and acts on both the drop and the liquid pool ( $t = 0.13 ms$ ). At the final stage  $t = 0.16 ms$  the interfaces are very close to each other ( $\sim 0.4 \mu m$ ) and the simulation is stopped. The bubble volume  $V_b$  can thus be determined

in Fig. 5.3, because no experimental data in this regime exists for drop impact onto a pool. We note that, just like results for drop impact onto flat plate [9],  $V_b$  exhibits a maximum. The physical reason for this maximum has been explained in Chapter 2. We note that  $V_b$  for drop impact onto a pool is also bigger than  $V_b$  for drop impact onto a flat plate in the capillary regime. To test the hypothesis of a factor 2, we plot  $0.5V_b$  instead of  $V_b$  for drop impact onto a pool. As can be seen in Fig. 5.6b, the yellow simulation data indeed collapses on the data which has only one deformable interface. These results thus support the following statement: the bubble that is entrapped during drop impact onto a pool is twice as big compared to impact which involves only one deformable interface. A more rigorous theoretical treatment is needed to further support this factor 2. Another explanation, which also successfully collapses the data in the inertial regime has been given by Tran et al. [6], which takes into account that the drop penetrates the pool with a penetration velocity  $U_p = 0.5U$ , where  $U$  is the impact velocity. When their experimental results for  $V_b$  for drop on a pool are plotted with a modified  $St$  based on  $U_p = 0.5U$ , the data in Fig. 5.6a is effectively moved to the left, which gives a similar collapse with the data with one deformable interface [6]. We check this experimental observation of  $U_p = 0.5U$  with our simulation data. A time evolution of the velocities of both interfaces at  $r = 0$  is shown in Fig. 5.7. After some transient behavior at time  $t = 0.1 ms$  where the drop is decelerated while the pool is accelerated, we see that both the drop and the pool adapt to half of the original impact speed, which is indicated with a solid line in the lower panel. This can be understood from an energy balance [6], which depends on the density ratio of the fluids, which is one in this case. This result demonstrates that BIM, apart from the microscopic air film entrainment, is also able to predict properties of the large scale dynamics of the problem.

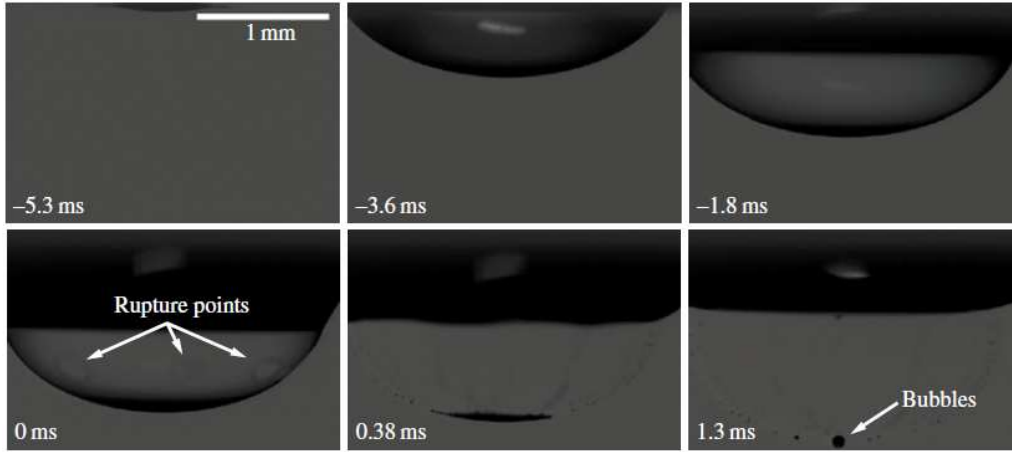


Figure 5.2: Adapted from Tran et al. [6]. A side view image sequence of a silicone drop with a viscosity of  $20 \text{ cSt}$  and a diameter of  $1.92 \text{ mm}$  entering a pool of the same liquid with an impact velocity of  $0.52 \text{ m/s}$  is shown. At  $0 \text{ ms}$  the air film ruptures and subsequently a bubble is trapped.

As Tran et al. [6] suggest in their work, it is interesting to investigate the effect of a density difference between the pool and the drop on  $U_p$ , which was not within the scope their work. However, this can be easily done with the current BIM, and could subsequently be verified with experiments. This is also not within the scope of this thesis, but recommended for future research. Furthermore, we note from Fig. 5.7, that the drop sinks very deep into the pool, compared to for example the drop in Fig. 5.1. It turns out that this actually depends on the impact speed  $U$  of the drop. The penetration depth of the drop into the pool will be the topic of the next section.

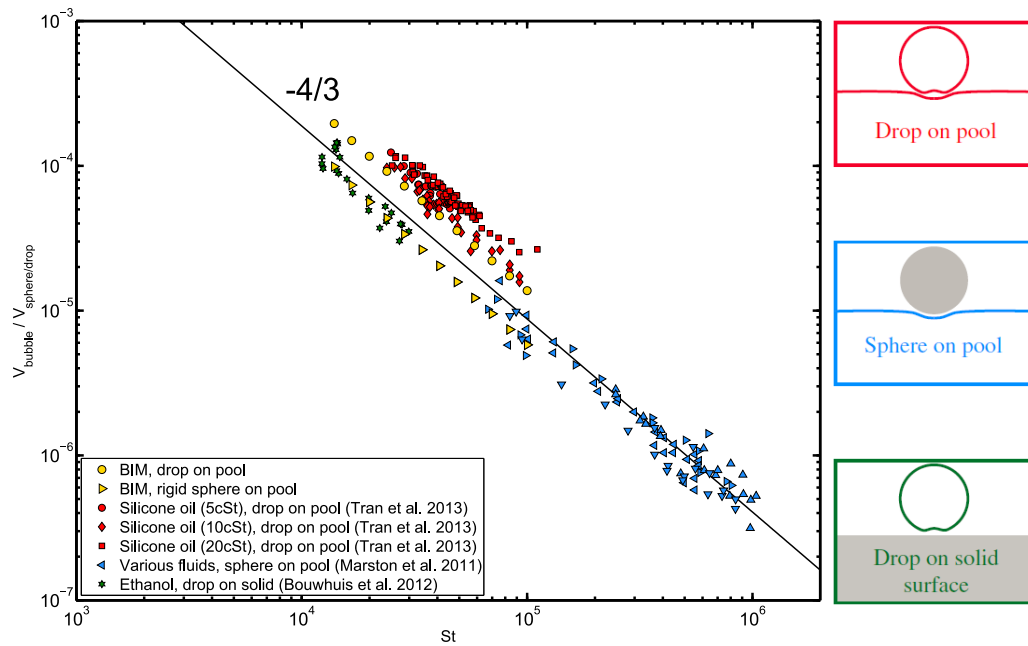


Figure 5.3: Figure adapted from Tran et al. [6], BIM results superimposed. Various experimental data for  $V_b$  is shown. As can be inspected from the figure,  $V_b$  for drop impact onto a pool is always bigger (almost perfectly a factor 2) compared to  $V_b$  of the sphere impact onto a pool and drop impact onto a solid.

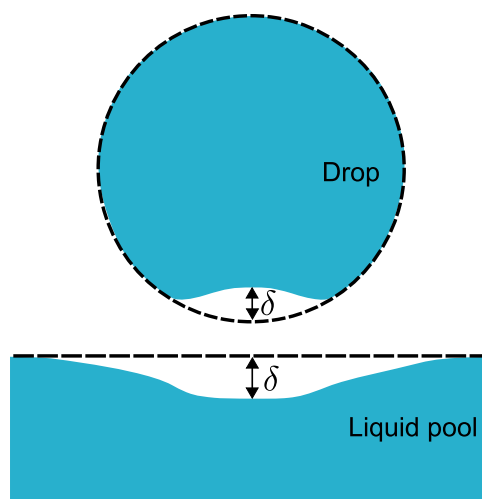


Figure 5.4: Definition sketch of  $\delta$

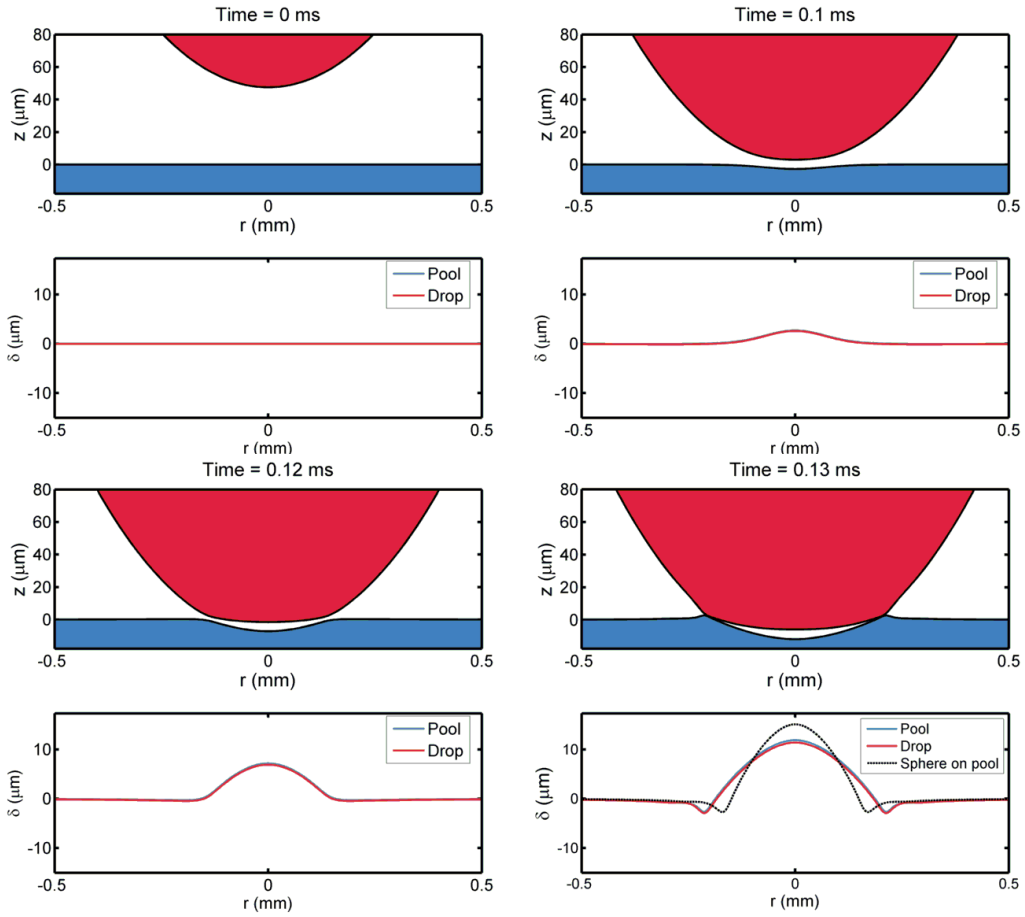


Figure 5.5: Drop impact onto a pool with a corresponding plot of the deformation  $\delta$  of both the pool and the drop. We observe excellent overlap between the deformations. In the final frame the deformation of the pool is shown in case of the impact of a rigid sphere instead of a drop for the same impact conditions: The impact speed is  $U = 0.42 \text{ m/s}$  and the radius is  $R = 0.95 \text{ mm}$ . The density and surface tension of the fluid are respectively  $\rho = 916 \text{ kg/m}^3$  and  $\gamma = 0.020 \text{ N/m}$ .

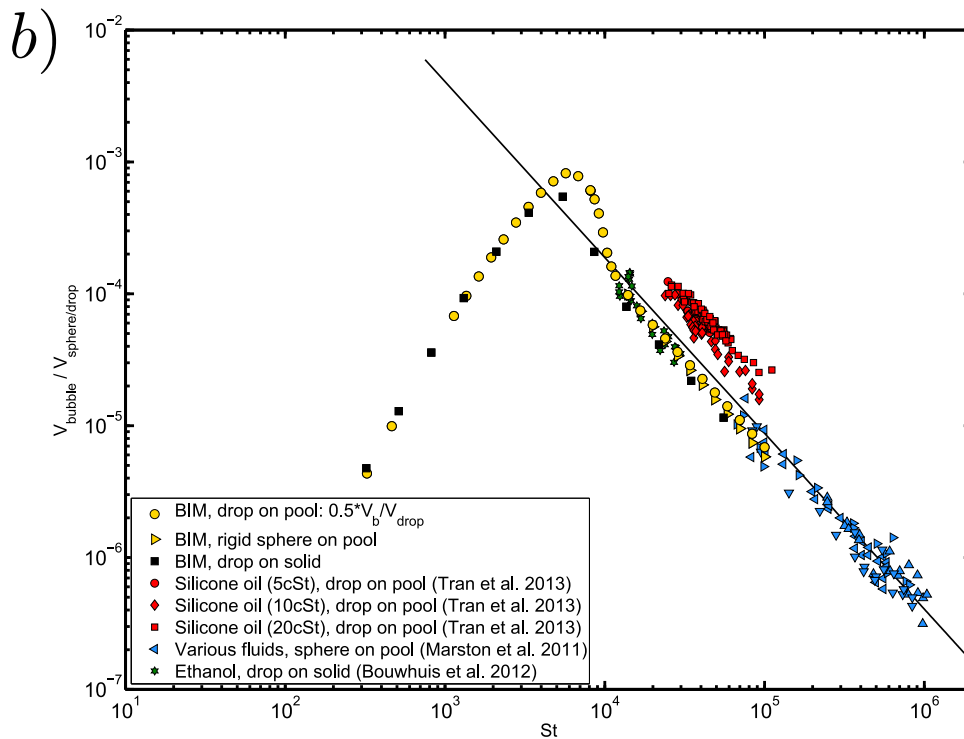
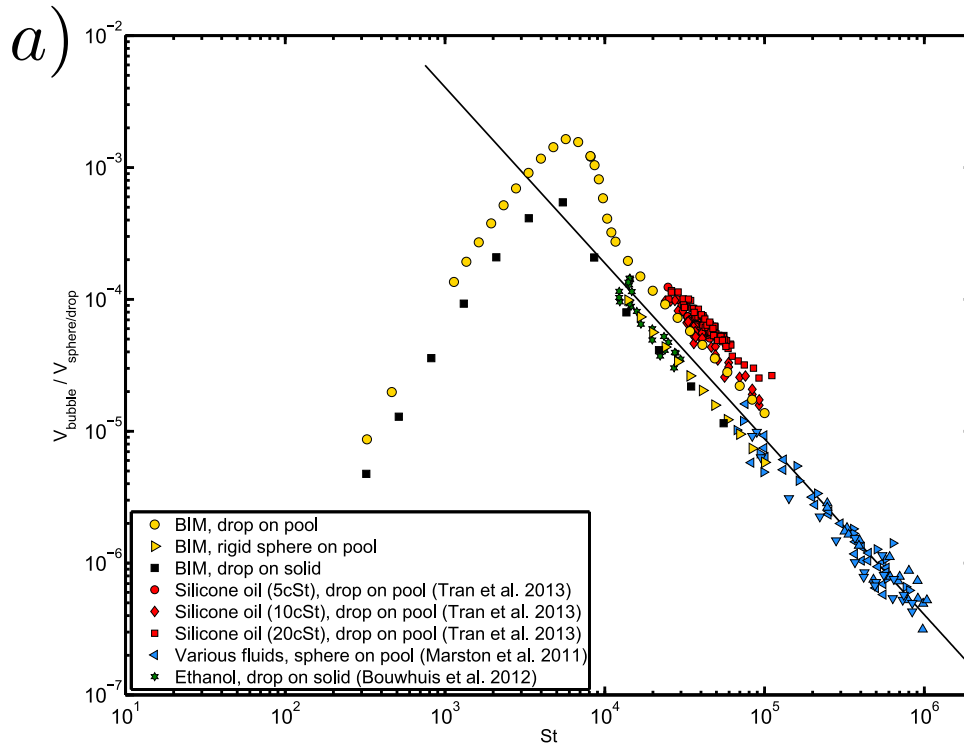


Figure 5.6: Figure adapted from Tran et al. [6], BIM results superimposed. a) Original data set b)  $V_b$  data for BIM (yellow circles) for drop impact onto a pool is multiplied by 0.5, and a collapse with the data with only one deformable interface is obtained.

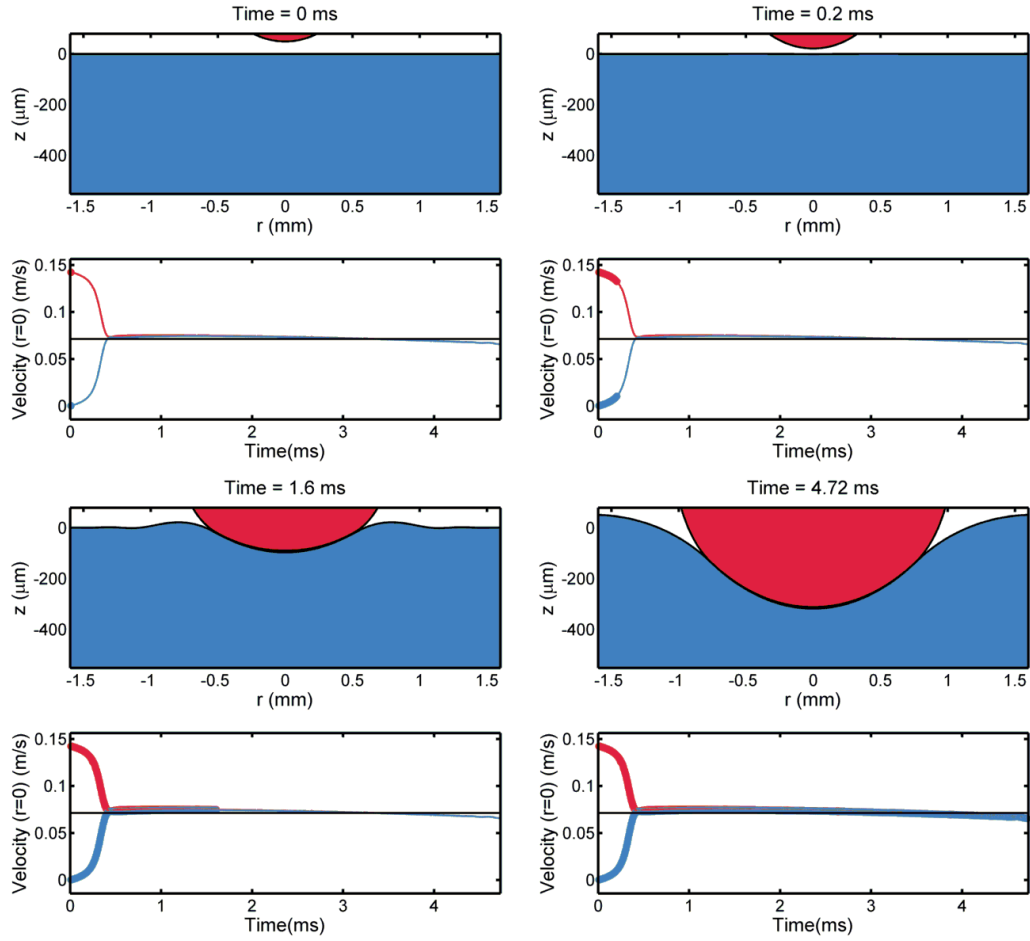


Figure 5.7: Drop impact onto a pool. The impact speed is  $U = 0.14 \text{ m/s}$  and the radius is  $R = 0.95 \text{ mm}$ . The density and surface tension of the fluid are respectively  $\rho = 916 \text{ kg/m}^3$  and  $\gamma = 0.020 \text{ N/m}$ . The vertical velocity of the two interfaces are tracked in time at  $r = 0$ . We observe that after some transient behavior the drop sinks with  $U_p = 0.5U$ , which is indicated with the black solid line.

## 5.2 Experimental results: penetration depth viscous drop onto a pool

In Chapter 5 we found very good agreement in the entrapped bubble volume during drop impact onto a pool when comparing BIM simulations to experiments. One difference between numerics and experiment was observed though, which is the penetration depth of the drop into the pool until rupture occurs. This distance is defined as the rupture height  $H_r$ , see Fig. 5.8. Here we focus on a set of experiments which have been carried out to investigate the effect of the viscosity of the liquid on  $H_r$ .

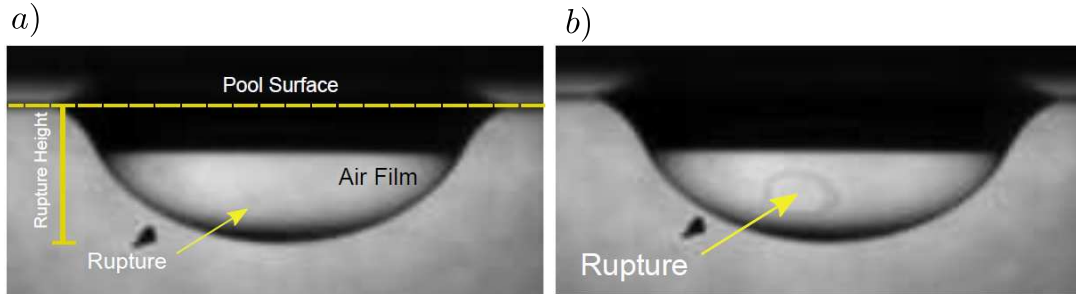


Figure 5.8: Courtesy of Ezeta and Citravidiya [20], who have made this image during the Experimental Technique course. a) A drop entering the pool right before air film rupture. b) Air film rupture is indicated with the yellow arrow.

The reason why the air film ruptures is that at some point the attractive van der Waals force between the surfaces becomes dominant which results in coalescence, which typically happens when the air film thickness is  $\sim 100\text{ nm}$  [21, 6, 7]. It turns out that  $H_r$  is greatly influenced by the material properties of the fluid that is employed, as is for example shown by Saylor et al. [22]. They showed that the use of viscous oils could result in relatively stable air films, which results in large  $H_r$ , compared to the case where they used water as the working fluid. In that case, no reproducible results regarding air film stability were obtained. Here it was hypothesized that possible surfactant contamination at the water surface is responsible for early coalescence, which inhibits reproducible experiments. Another phenomenon that can be observed is that a drop with a low enough impact speed bounces back after entering the pool. In that case no rupture of the air film occurs, and the drop is able to bounce back. Thoroddsen et al. [7] demonstrated that the threshold impact velocity for bouncing depends on the viscosity of the liquid. This demonstrates again the importance of liquid properties on the onset of rupture. We further investigate the effect of impact velocity and viscosity on  $H_r$  in a more complete parameter scan. A setup, which is schematically shown in Fig. 5.9, is used to acquire high-speed image sequences of a drop that impacts on a pool of the same liquid. An example of a typical image that is taken by the high-speed camera is depicted in Fig. 5.8. From this image  $H_r$  can be measured. Before the drop hits the pool, the drop is still undeformed and the diameter and impact velocity can be furnished from the recording (not shown in Fig. 5.8).

To investigate the effect of viscosity, different types of silicone oil have been used, see Table 5.1. The experimental result for  $H_r$  as function of  $St$  is depicted in Fig. 5.10 of four different viscosities is shown. The BIM results are also included in this plot. As can again be noticed from this plot, numerical results for  $H_r$  are much smaller than the experimental result for  $H_r$ . But we note as well that, when looking at the experimental data, the viscosity of the silicone oil also affects  $H_r$ . From the data we can see a trend that for the same  $St$  the rupture height  $H_r$  will be bigger for a more viscous oil. But apparently this doesn't affect the bubble volume that is entrapped, as after close inspection of Fig. 5.3, the  $V_b$  versus  $St$  data don't show a trend as a function of the different viscosities that were used for the experiments of drop impact onto a pool. This again supports the hypothesis that the bubble volume of an impacting object onto a pool is already determined in the early stage, as was also discussed in Chapter 4. The reason why  $H_r$  depends on the viscosity of the silicon oil has probably to do with the chemical properties of the particular silicon oil, and this hypothesis could be a topic for future research.

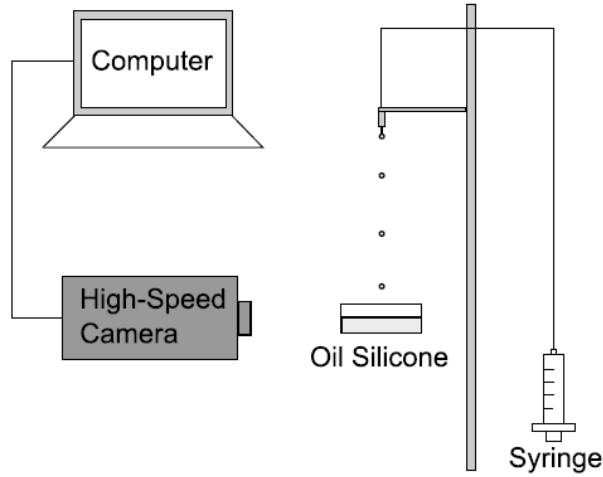


Figure 5.9: Courtesy of Ezeta and Citravidya [20], who have made this image during the Experimental Technique course. Schematic of the experimental setup that was employed to study the rupture height  $H_r$ . A high speed camera (Photron Inc.) is triggered with the computer to capture individual drop impact events. By adjusting the height of the needle (24-gauge stainless steel needle, Hamilton Co) the impact velocity of the drop could be varied. This allows for a systematic parameter scan covering different impact velocities.

	Density ( $\rho$ ) [ $kg/m^3$ ]	Surface tension ( $\gamma$ ) [ $N/m$ ]
5 cs	916	$19.7 \times 10^{-3}$
10 cs	934	$20.1 \times 10^{-3}$
20 cs	953	$20.8 \times 10^{-3}$
50 cs	963	$20.8 \times 10^{-3}$
100 cs	968	$20.9 \times 10^{-3}$

Table 5.1: Physical values for each of the used oils and average diameter of the droplets.

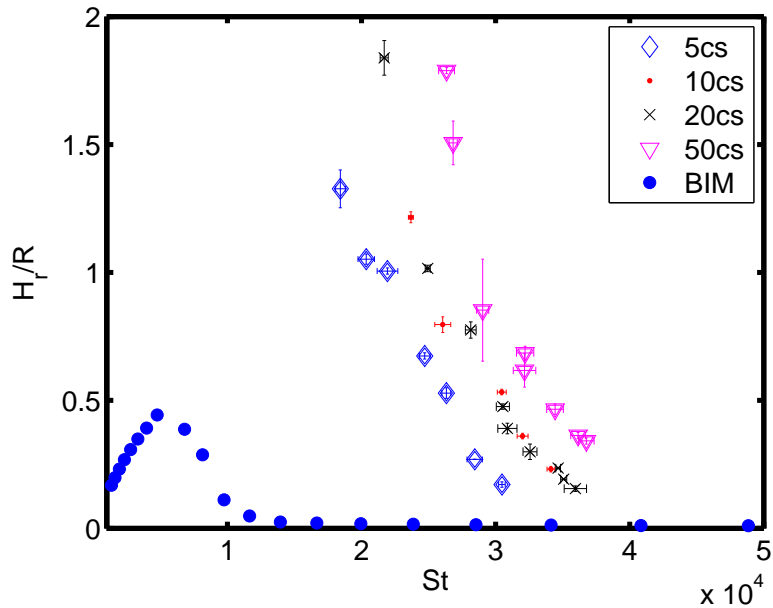


Figure 5.10: Courtesy of Ezeta and Citravidya [20], who have made this image during the Experimental Technique course. Experimental results for the rupture height  $H_r$  versus  $St$ . BIM results are superimposed.

## Chapter 6

# Air film dynamics during drop impact onto hydrophobic micro-patterned surfaces

In the previous chapters only axisymmetric 2d impact phenomena have been modeled with BIM and compared with experiments. A full 3d BIM simulation of the fluid coupled to the viscous air layer, as has been done for example by Hicks et al. [18], is not within the scope of the present thesis. However, recent advances in high-speed color interferometry [10] allows us to quantify airfilm dynamics during a 3d impact event experimentally. We will focus on the use of this interferometric technique to analyze the 3d airfilm dynamics of the thin air layer that is trapped between an impacting drop and a hydrophobic micro-structure. During my master project I became involved in this experimental project, which is not directly related to the numerics of impact onto pool, which is the main focus of the thesis. This chapter is based on a preprint authored by R.C.A. van der Veen, M.H.W. Hendrix, T. Tran, P. Tsai, C. Sun, and D. Lohse [23]. My contributions to this project were doing measurements and doing analysis. We start with a section describing the experimental details before continuing to the results of the analyzed air film.

### 6.1 Experimental details

As described in Chapter 2, a drop impacting onto a solid causes the air pressure underneath the drop to increase due the thin air layer that needs to be squeezed out before the drop can touch the solid. This build-up of air pressure can deform the drop, causing a non-equilibrium dimple, which may result in air bubble entrainment [24, 25, 26, 9]. The role of air has shown to be important in the macroscopic splashing behaviour of droplets impacting on smooth surfaces [27] or micro-structured surfaces [28]. In the latter case, the interplay of the trapped air and the geometry of the structure determine the complex outcome of a drop impact event, such as directional splashing. A characterization of the dynamics of the airfilm during drop impact onto a microstructured surface has however not been obtained before, to the author's best knowledge, and is it is therfor essential to quantify these dynamics.

When a drop impacts onto a microstructured surface instead of a smooth surface we have the same mechanism of increasing air pressure that will deform the drop, see Fig. 6.1d. In this case however, we do not deal with a smooth surface and we expect that the micropillar morphology on the glass slide influences the airfilm dynamics. We focus on the trapped air layer between an impacting water drop and various superhydrophobic micro-structured surfaces. We quantitatively measure the air film thickness during impact, using the color interferometry method which has been recently used to infer the dynamics of the air film under an impacting drop onto a smooth surface [10]. The experimental method together with a description of the microstructure is depicted in Fig. 6.1.

The experimental setup is shown in Fig. 6.1a and is similar to that of [9, 10], with the exception of the use of hydrophobic micro-patterned surfaces. A milli-Q water drop detaches from a needle after growing quasi-statically and impacts on the surface. A high-speed side view recording is used to measure impact velocity and droplet diameter. The targeted substrate consists of glass micropillars regularly arranged in a square lattice, with pillar width  $W$ , pillar spacing  $S$  and pillar height  $H$ , as shown in Fig. 6.1a, b. It is coated with a hydrophobic fluorocarbon (FC) coating [29], which gives a contact angle of  $113^\circ$  for

water on glass. The thickness of this film is around the order of 100 nm. Micro-patterned surfaces with hydrophilic coatings were also tried, but found to be less suitable to study impact dynamics and compare with the case of smooth glass slides (Menzel microscope slides, average roughness  $\approx 10$  nm). Because the pillar heights are of the order of the thickness of the typical air layer, the liquid touches the pillars early in the impact process and consequently quickly completely wets the surface. In the case of hydrophobic pillars the liquid first only wets the top of the pillars (see Fig. 6.2a) and is pinned at the top pillar edge (see Fig. 6.5d). This allows the dimple dynamics to be compared with the smooth surface case. The hydrophilicity of the smooth glass slides does not influence the pre-wetting phenomena because there is no contact between the liquid and surface. A synchronized bottom view recording by a high-speed color camera is used to measure the shape of the bottom of the droplet, or equivalently, the shape of the air film between the droplet and the surface. Broad-spectrum white light from a high-intensity mercury vapor lamp (Olympus ILP-1) is fed into the coaxial light port of the long-working-distance microscope (Navitar inc.). This light reflects from both the top surface of the substrate and the bottom surface of the droplet (see Fig. 6.1(e)), creating colored interference patterns. These colored patterns can be used to measure the absolute thickness of the film in question, since the color of the interference at a certain location is determined by the local filmheight  $h$ . A color-matching approach in combination with known reference surfaces is employed [10].

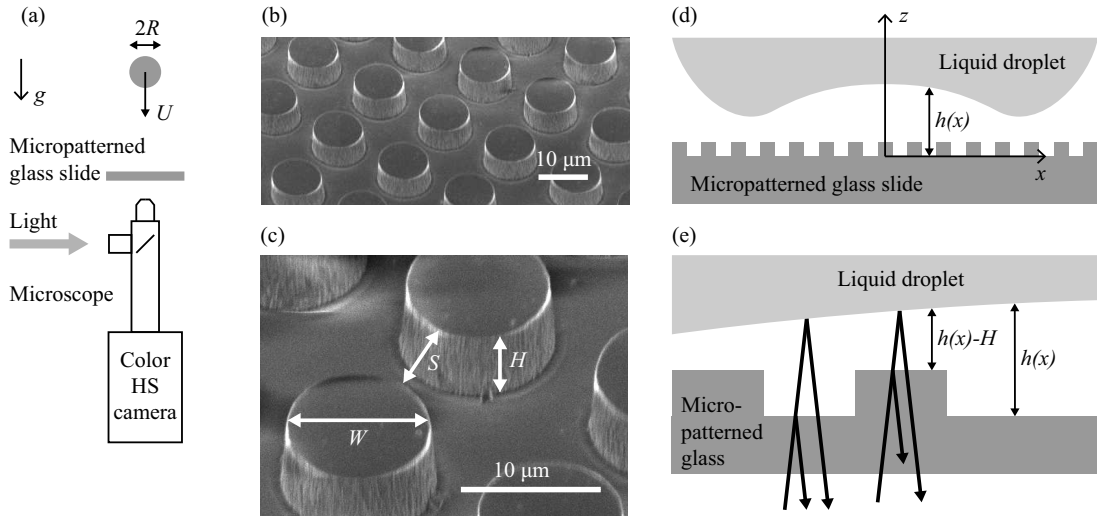


Figure 6.1: Experimental characterization of the drop impact experiments. (a) Schematic of the experimental setup used to study drop impact using high-speed color interferometry. A water droplet with a typical radius of  $R = 1$  mm falls on a transparent hydrophobic micropatterned or hydrophilic smooth glass slide. The impact velocity can be varied by changing the falling height of the droplet, but is typically  $U = 0.4$  m/s. The droplet radius and velocity is measured using a high-speed side view camera (not shown). The bottom view is captured by a high-speed color camera (SA2, Photron Inc.) operating at 10000 or 20000 frames per second (FPS). The camera is connected to a long working-distance microscope and a 10x objective to obtain a 1 mm field of view. (b) Scanning electron microscope (SEM) image of a representative micropatterned surface used in the drop impact experiments. (c) Magnified SEM image showing the width ( $W$ ), spacing ( $S$ ) and height ( $H$ ) of the micropillars. (d) Sketch of the dimple formation (not drawn to scale) just prior to impact. The height  $h(x)$  of the air film is defined from the bottom of the pillars to the bottom of the liquid drop. (e) Schematic showing the interference of light rays between the glass micropatterned surface and the liquid droplet. Light can interfere both in between and through the transparent pillars; refer to Fig. 6.2(a) for an example of an interference pattern.

## 6.2 Characteristics of airfilm

The resulting air layer shape of impact on a substrate with relatively large pillar width and spacing is shown ( $W = 100 \mu\text{m}$ ,  $S = 100 \mu\text{m}$ ) in Fig. 6.2. As is the case with smooth surfaces, the liquid is deformed and a dimple is created due to a pressure build-up in the air layer. In Fig. 6.2(b) it can be seen that this also happens very locally; above one of the pillars a local maxima in the air layer thickness is formed.

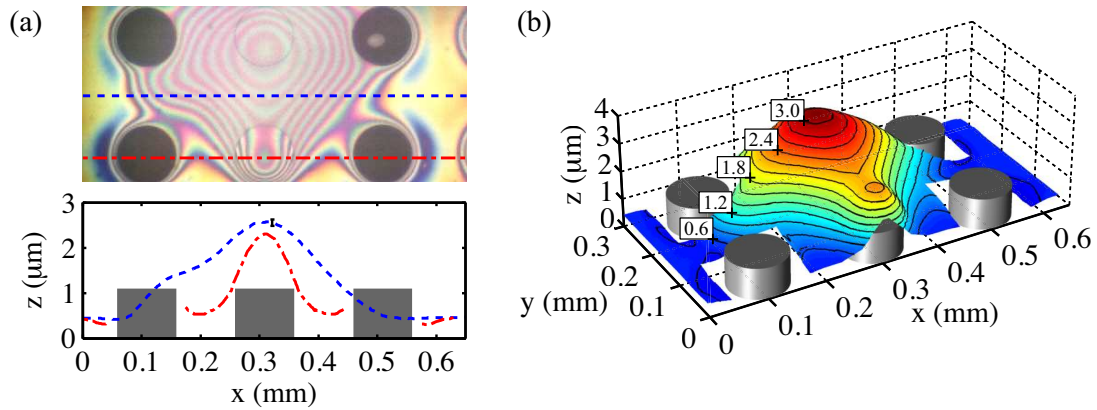


Figure 6.2: Two-dimensional (2-D) and three-dimensional (3-D) reconstruction of the air layer profile between an impacting droplet and micropatterned surface. The droplet radius is  $R = 1$  mm, the impact velocity is  $U = 0.4$  m/s, the micropattern properties are  $W = 100 \mu\text{m}$ ,  $S = 100 \mu\text{m}$ ,  $H = 1.1 \mu\text{m}$ . (a) Top: Snapshot of the interference pattern created by light interfering between the surface and the bottom of the droplet. The liquid wets the top of four of the six visible pillars. The pillars are large compared to the dimple width, resulting in broken symmetry. Bottom: Air layer profiles along two lines shown at the top. Take note of the difference in horizontal and vertical scale. (b) 3-D reconstruction of the air layer. Black iso-height lines are shown with labels in  $\mu\text{m}$ . The dimple is deformed by the presence of the micropillars.

In the case of smaller pillar width and spacing, the air layer shapes and impact dynamics are much more reminiscent of impact on a smooth surface, see Fig. 6.3. A cross-section of the air layer is made through the space between two rows of pillars. Two distinct areas can be discerned. One is the dimple which is very symmetrical and not influenced by the presence of the pillars. The second one is the outer region where the top of the pillars are wetted and the liquid bends down into the gaps to a height of approximately  $0.3 \mu\text{m}$ , less than half of the pillar height. In between, there is a connecting region of colored rings where the height of the film decays from the pillar height to the mentioned penetration height  $0.3 \mu\text{m}$ . At an unpredictable time the liquid unpins (outside of the frame) from the pillars and starts to completely wet the surface. As can be the case with smooth surfaces, the dimple collapses into an entrapped air bubble. The time at which wetting starts varies between experiments, because it strongly depends on small irregularities or contaminants. Together with possible tiny tilts or non-symmetrical release of the droplets these effects also cause the non-axisymmetric wetting behavior.

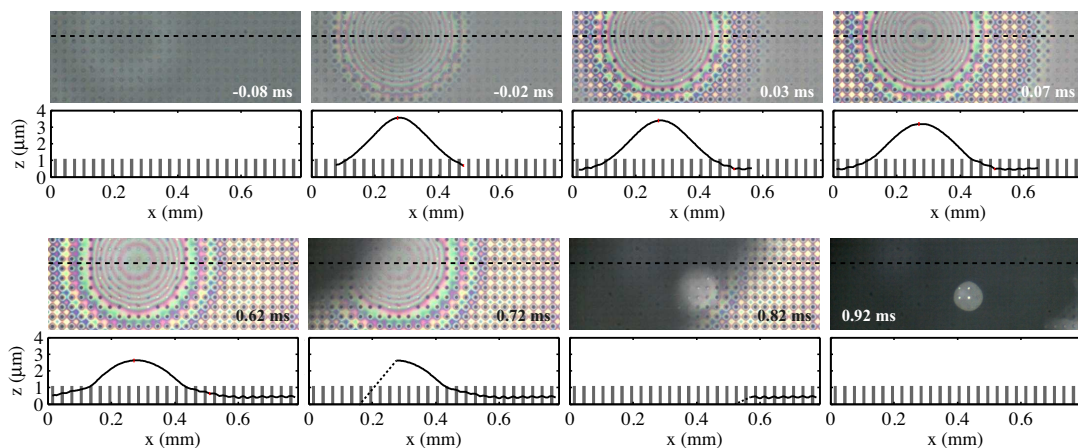


Figure 6.3: Snapshots of interference patterns and their corresponding calculated profiles obtained during impact ( $U = 0.4$  mm/s,  $R = 1$  mm) on a micropatterned surface ( $W = 10 \mu\text{m}$ ,  $S = 20 \mu\text{m}$ ,  $H = 1.1 \mu\text{m}$ ). Take note of the large time step between the fourth and fifth frame. At 0.72 ms wetting starts, resulting in a stable entrapped air bubble.

To study the effect of the micropillar size and arrangement, we measure the height of the air film at the center of the dimple. In Fig. 6.4(a) it can be seen that the dimple shape itself is quite symmetrical for all pillar arrangements considered. By counting the fringes one can already note that the dimple height is different for every arrangement. This is quantified in Fig. 6.4(b) by plotting the dimple height  $H_d(t)$  versus time for six different micropillar arrangements and one smooth surface case. Time  $t = 0$  is defined at the moment where fringes are first visible in the frame. The first thing to notice when comparing the dimple height evolutions is that all have very similar shape and seem to be shifted vertically with respect to each other. This is quantified in Fig. 6.4(c), where the difference of all profiles with the smooth surface case is shown. In an interval of 0.2 ms the fluctuation of these lines is within the measurement error of 100 nm. The presence of protruding pillars in the air layer creates an additional pressure build-up, or resistance, to the impacting droplet, increasing the height of the dimple. For equal pillar width and smaller pillar spacing, the dimple is pushed up higher because air can escape less easily. Outside of the dimple, the liquid wets the top of the pillars, so there are only channels with cross-sectional area of less than  $S \cdot L$  through which air can escape. When comparing cases with equal ratio of pillar spacing to pillar width  $S/W$ , the total area through which air can escape is equal. Nonetheless, structures with larger dimensions have a smaller dimple height suggesting that air escapes more easily in those cases. This can be explained using the concept of hydrodynamical resistance (aerodynamical in this case), which is larger for many small channels than for a smaller number of large channels with equal total cross-sectional area. The geometrical parameter  $W/(W + S)$  is used to show the dimple height increase depending on the micropillar arrangement (Fig. 6.4(d)). This factor includes smooth surfaces at 0 and 1, shifted by the pillar height in question. The three different values show a monotonic increase between 0 and 1. Further exploration of pillar arrangements could supply a scaling dependence between dimple height increase and pillar geometry, possibly also including the air flow resistance to collapse the data.

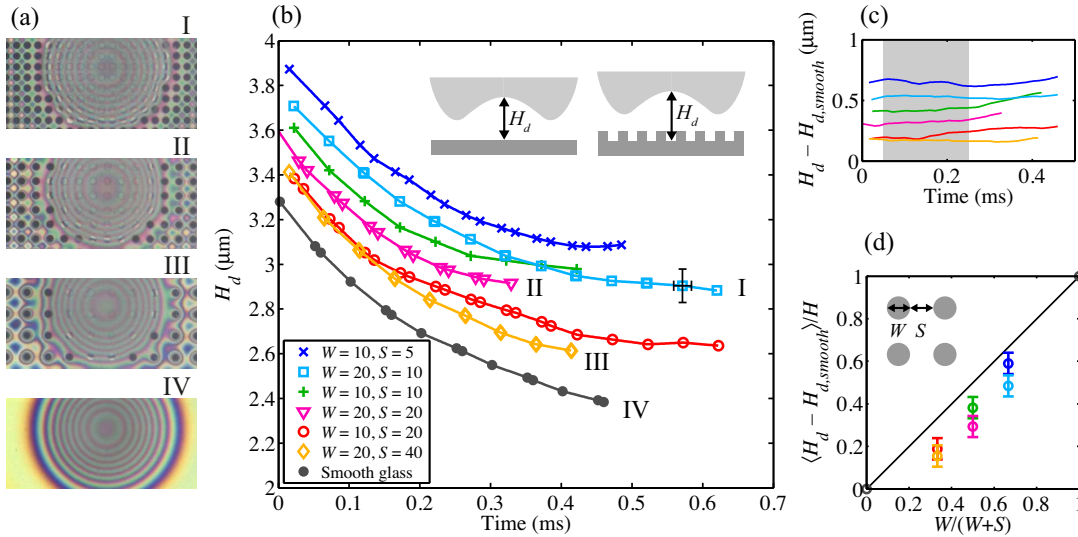


Figure 6.4: Overview of micropattern dependence for fixed pillar height  $H = 1.1 \mu\text{m}$  ( $U = 0.4 \text{ m/s}$ ,  $R = 1 \text{ mm}$ ). (a) Four snapshots at  $t = 0.23 \pm 0.03 \text{ ms}$  (see text for definition of reference time) of micropatterned surfaces ( $W = 20 \mu\text{m}$ ) with spacings  $S = 10, 20$  and  $40 \mu\text{m}$  and one smooth glass slide. (b) Evolution of maximal dimple height with time. Every line consists of an average of two individual experiments, which are independently shifted in time according to the method described in the text. The variation between every experiment falls within the systematic error of 150 nm we attribute to the method of analysis. (c) The difference between the six micropattern experiments and the smooth surface case, showing that the shape of  $H_d(t)$  hardly depends on the type of micropattern. The gray area shows the interval  $0.05 \text{ ms} < t < 0.25 \text{ ms}$  used to determine the average dimple height difference. (d) Average dimple height difference normalized by the pillar height  $H = 1.1 \mu\text{m}$  versus the pillar width parameter  $W/(W + S)$ . A value of zero corresponds to a smooth surface at  $z = 0$ , a value of one corresponds to a smooth surface at  $z = H$ . The wider the pillars compared to the unit cell, the higher the air dimple. Besides this, the smaller the absolute spacing, the higher the dimple height.

Besides the pillar width and spacing, influence of pillar height is also of interest. Fig. 6.5(a) through (c) show snapshots of the interference patterns and corresponding dimple shapes for three different pillar

heights. For a pillar height  $H = 1.1 \mu\text{m}$ , which is smaller than the typical dimple height, the dimple is not disturbed and still symmetric. For larger pillar heights the liquid wets the top of all the pillars and the dimple is much more deformed, although the general shape can still be seen. As a further indication that the liquid is pinned at the top of the pillars, a profile between two adjacent pillars is constructed (Fig. 6.5(d)). A combination of the color interference technique and manually counting fringes allows us to resolve a large part of the fringes in between the pillars. Very close to the pillars the profile is steep and the fringes are too narrow to resolve. Profiles at two instants in time both show, when extrapolating, that the liquid surface is connected very close to the top of the pillars. .

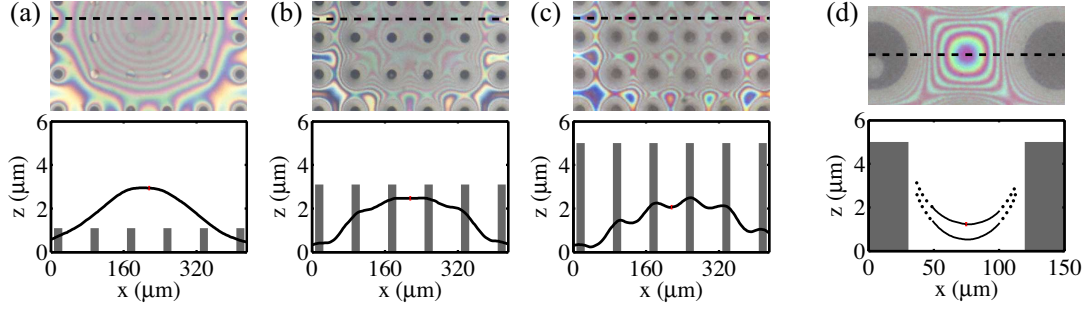


Figure 6.5: Influence of pillar height. (a), (b) and (c) Snapshots of measurements at  $t = 0.15 \pm 0.03$  ms with  $W = 20 \mu\text{m}$  and  $S = 60 \mu\text{m}$ , but different pillar heights of  $H = 1.1, 3.1,$  and  $5 \mu\text{m}$  respectively ( $U = 0.4$  m/s,  $R = 1$  mm). The profile is evaluated along a line between the pillars, showing that especially for large pillar height the air film significantly penetrates the microstructure. The dimple height and volume do not seem to clearly depend on the pillar height. (d) Top: Magnification of interference pattern between two pillars at  $t = 0.23 \pm 0.03$  ms ( $U = 0.3$  m/s,  $R = 1$  mm,  $W = 50 \mu\text{m}$ ,  $S = 50 \mu\text{m}$ ,  $H = 5.1 \mu\text{m}$ ). Bottom: Air layer profile for  $t = 0.3$  ms and  $t = 2.3$  ms. The separate data points are measured by selecting the fringes by hand, while the center part is done using the color interference technique described in the text. The shape and dynamics of this pattern suggest pinning of the liquid to the top edge of the pillars.

# Chapter 7

## Discussion and outlook

In this final chapter we reflect back on the findings of this thesis and discuss possible opportunities for future research.

### 7.1 Discussion

Theory for drop impact onto a solid plate has been extended to describe and quantify air entrainment during the impact of a rigid sphere onto a liquid pool and drop impact onto a liquid pool. The fluid was modeled with potential flow, using the Boundary Integral Method (BIM), coupled to viscous lubrication theory for the surrounding air, which needs to be squeezed out at the impact zone. For the case of drop impact onto a pool, two distinct domains were successfully created in the existing BIM code for one fluid domain. Air bubble entrainment for both rigid sphere and drop impact onto a liquid pool have been found to agree excellent with experimental data and theory, as has been shown in Chapter 4 and Chapter 5.

The distance that the impacting sphere or drop travels into the pool before the air film between the two interfaces ruptures is however not agreeing when comparing numerics to experiment. As results have shown in Chapter 5.2, this penetration distance is for experiments typically much larger than for numerics. As the complex interaction energy between the two interfaces in the final stage determines rupture in experiments, it will be very hard to capture this in a numerical model, since whole new physics enter at small scale separations of  $\sim 100\text{ nm}$ . Therefore, in the current situation, a minimum numerical air thickness is chosen to account for rupture: at a minimum air film thickness of  $0.4\ \mu\text{m}$  the simulation is stopped and rupture is assumed. This introduced cut off might be the reason for the discrepancy between experiment and theory regarding the penetration distance. Another reason for the discrepancy could be that in the early stage of impact the inertia of the air plays a role in deforming the pool, which is not captured in the model, since viscous lubrication theory is used to describe the air layer. The difference in penetration distance, however, doesn't seem to effect the final air bubble volume, as is also suggested by Thoroddsen et al. [3] for impact of a rigid sphere onto a pool, where it was showed that the bubble volume is determined at early stage of impact. To further attest this hypothesis for drop impact onto a liquid pool, experiments have been conducted with silicon oils of varying viscosity, which showed different penetration distances depending on the viscosity of the oil: a trend could be observed that more viscous silicon oil drops have a larger penetration distance over the whole range of impact velocities that were explored, see Chapter 5.2. Experimental results for drop impact onto a pool, which have also been discussed in Chapter 5.1, show that different viscosities don't affect the bubble volume [6], which supports our hypothesis that the penetration distance is not determining the entrapped bubble volume. Furthermore, the penetration velocity  $V_p$  of the drop into the pool has been numerically investigated, and was found to be  $V_p = 0.5V$  where  $V$  is the impact speed of the drop. This agrees with experimental findings of Tran et al. [6]. In addition, the behavior of the microscopic air film that is trapped during drop impact onto a hydrophobic micro structure is characterized experimentally, making use of high-speed color interferometry.

### 7.2 Outlook

In this thesis only axisymmetric impacts are modeled. It would be a challenge to extend the model to a 3d version to capture for instance the complex 3d dynamics of an impacting drop onto a micro structure,

as has been experimentally investigated in Chapter 6. It is emphasized that this will be challenging since both the BIM for potential flow and the viscous lubrication equations have to be modified to a 3d version. Hicks and Purvis [18] have however already been able to account for the 3d dynamics of a drop and the trapped air layer in the case where a drop impacts onto a non-flat surface. Here also a BIM for the impacting drop was coupled to the dynamics of the air layer. In this thesis we have mainly considered the inertial regime, where surface tension effects could be neglected. However, as is also shown in Chapter 2, experiments and BIM don't agree with the scaling for the entrapped bubble volume, Eq. 2.2:  $V_b/V_{drop} \sim St$  in the capillary regime, see also Fig. 7.1a.

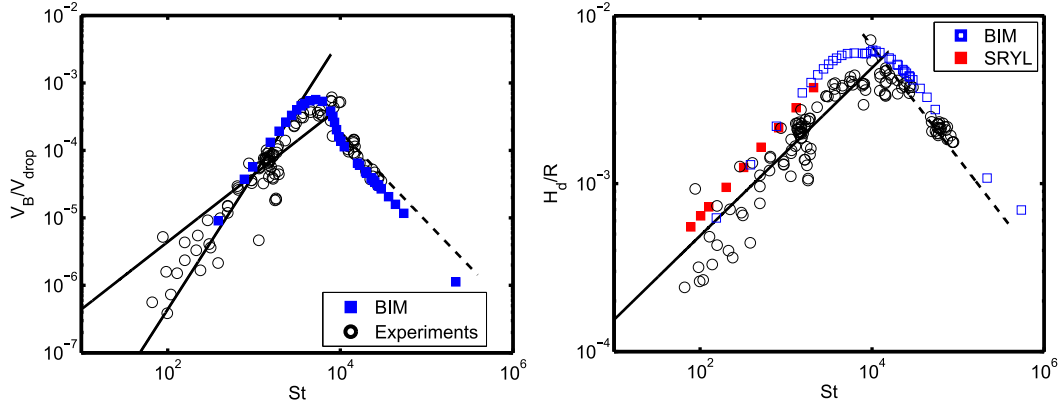


Figure 7.1: a) Adapted from Bouwhuis et al. [9]. a) Normalized bubble volume  $V_b/V_{drop}$  versus  $St$ . Blue symbols correspond to BIM results, black open circles correspond to experimental data. b) Normalized dimple height  $H_d/R$  versus  $St$ . SRYL results are superimposed on existing experimental and BIM data and show excellent agreement.

We observe that the BIM results in the capillary regime give a slope of 2, instead of 1 which is predicted on basis of scaling theory [9] which is based on a balance between capillary pressure and lubrication pressure. This leads us to the suspicion that it might be the case that inertia is still playing some role in the BIM simulations in the capillary regime. One could think of performing BIM simulations where the density is put to a very low value to test if only capillary effects remain. This is, however, also counter-intuitive, since BIM for potential flow assumes high Reynolds number flows, so putting the density to a very low value cannot be done without some checks. Also, BIM simulations in the capillary regime take typically 10 times more CPU time compared to the inertial regime, because the impact speeds are relatively low. This motivates us to look for a simpler model that takes the capillary effects into account, and doesn't have inertia in it. Stokes-Reynolds-Young-Laplace (SRYL) theory is meeting these needs, which is described in detail in Appendix B. An advantage of this model is that a typical simulation takes minutes, whereas the corresponding BIM simulation takes days. SRYL theory also suggests  $V_b/V_{drop/sphere} \sim St$  and  $H_d/R \sim St^{1/2}$ , just as is derived by Bouwhuis et al. [9]. As can be observed in Fig. 7.1b, SRYL results are in agreement with BIM results and experiments, and also the theoretical scaling  $H_d/R \sim St^{1/2}$ . As is explained in Appendix B it is not possible yet to determine  $V_b$  with the current SRYL theory, because only the local deformation of the drop at the impact zone is solved in the early time, which doesn't result in a bubble yet, see Appendix B. Further development of this theory would be recommended, to see if a bubble is entrapped in a later stage, and how it will relate to the present findings. It will be needed to link the inner problem to the outer drop shape, as is for example done in Chan et al. [30], to ensure volume conservation of the drop.

For future research, it would be interesting to investigate the dynamics of a drop that impacts onto a thin liquid layer instead of an infinite liquid pool. Viscous effect in such a thin film may become important, and BIM cannot be used to model such a viscous film, since inviscid flow is assumed in the BIM for potential flow framework. In that case another tool needs to be used to account for the full equations that are needed to describe the dynamics of this liquid film, such as the open-source Gerris software [31]. With the newly arisen possibility to work with more than one liquid domain in the BIM code, new possibilities are opened to study problems with more than one liquid domain. It would be also interesting to continue simulation of a drop impacting onto a pool after the air film is ruptured. This would require a recombination of the two liquid domains, which is not done in this work yet. Rather, this is recommended for future research.

# Appendix A

## Stokes flow in cylindrical coordinates

To derive the lubrication equation for Stokes flow in the air gap we start by considering the initial geometry of the problem which is depicted in Fig. A.1. This geometry is identical for drop impact onto a flat plate, drop impact onto a liquid pool, and impact of a rigid sphere onto a pool. For doing this lubrication analysis we follow references [32, 33].

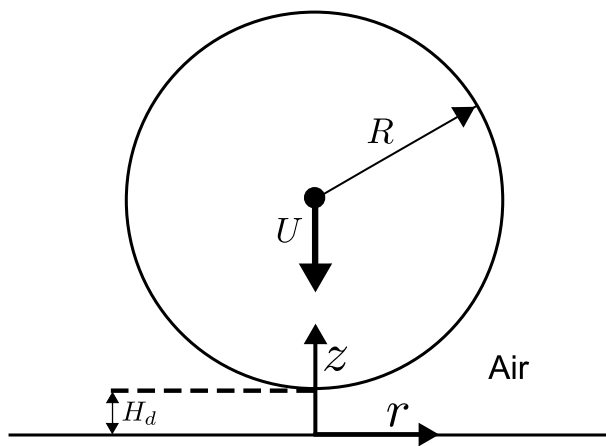


Figure A.1: Schematic of drop impact onto a solid plate

We will introduce scaled dimensionless variables to help us identify which terms are dominant in the governing physics of our problem. We will make use of the parameter  $\epsilon = H_d/R \ll 1$ , exploiting the fact that the two lengthscales  $H_d (\sim \mu m)$  and  $R (\sim mm)$  in this problem differ three orders of magnitude. Dimensionless variables will be indicated with an asterisk. We first scale the coordinates  $r$  and  $z$ . A natural scaling for  $z$  will be the typical height of the air gap  $H_d$ :  $z^* = z/H_d = z/R\epsilon$ . To find a proper scaling for  $r$ , we take into account the shape of the sphere, which can be approximated with a parabola:

$$z = H_d + \frac{r^2}{2R}. \quad (\text{A.1})$$

Using this formula together with the scaling for  $z^*$ , we deduce  $r^* = r/R\epsilon^{1/2}$ . Similarly, a natural scale for  $u_z^*$  would be:  $u_z^* = u_z/U$ . The continuity equation Eq. A.2 with dimensionless variables  $r^*, z^*$  and  $u_z^*$  is given by:

$$\frac{1}{R\epsilon^{1/2}} \frac{1}{r^*} \frac{\partial(r^* u_r)}{\partial r^*} + \frac{U}{R\epsilon} \frac{\partial u_z^*}{\partial z^*} = 0. \quad (\text{A.2})$$

We deduce that  $u_r^* = u_r \epsilon^{1/2}/U$ , since both terms of Eq. A.2 have to be of the same order [33]. The flow of the air film will obey the Navier-Stokes equation. The  $r$ -component of the Navier-Stokes equation in cylindrical coordinates for axisymmetric flow, neglecting gravity, is given by:

$$\rho \left( \frac{\partial u_r}{\partial t} + u_r \frac{\partial u_r}{\partial r} + u_z \frac{\partial u_r}{\partial z} \right) = -\frac{\partial p}{\partial r} + \mu \left( \frac{\partial^2 u_r}{\partial z^2} + \frac{1}{r} \frac{\partial}{\partial r} \left( r \frac{\partial u_r}{\partial r} \right) - \frac{u_r}{r^2} \right) \quad (\text{A.3})$$

This equation can also be written non-dimensionalized using the previous defined dimensionless variables, together with the scaled time  $t^* = tU/R\epsilon$  and scaled pressure  $p^* = pR\epsilon^2/\mu U$  to give:

$$\frac{\rho U^2}{\epsilon^{3/2} R} \left( \frac{\partial u_r^*}{\partial t^*} + u_r^* \frac{\partial u_r^*}{\partial r^*} + u_z^* \frac{\partial u_r^*}{\partial z^*} \right) = -\frac{\mu U}{R^2 \epsilon^{5/2}} \frac{\partial p^*}{\partial r^*} + \mu \left( \left( \frac{U}{R^2 \epsilon^{5/2}} \right) \frac{\partial^2 u_r^*}{\partial z^{*2}} + \left( \frac{U}{R^2 \epsilon^{3/2}} \right) \frac{1}{r^*} \frac{\partial}{\partial r^*} \left( r^* \frac{\partial u_r^*}{\partial r^*} \right) - \left( \frac{U}{R^2 \epsilon^{3/2}} \right) \frac{u_r^*}{r^{*2}} \right) \quad (\text{A.4})$$

Now we divide by the coefficient of the biggest visous term,  $\mu U/R^2 \epsilon^{5/2}$ , to obtain:

$$\frac{\rho U \epsilon R}{\mu} \left( \frac{\partial u_r^*}{\partial t^*} + u_r^* \frac{\partial u_r^*}{\partial r^*} + u_z^* \frac{\partial u_r^*}{\partial z^*} \right) = -\frac{\partial p^*}{\partial r^*} + \left( \frac{\partial^2 u_r^*}{\partial z^{*2}} + \epsilon \frac{1}{r^*} \frac{\partial}{\partial r^*} \left( r^* \frac{\partial u_r^*}{\partial r^*} \right) - \epsilon \frac{u_r^*}{r^{*2}} \right) \quad (\text{A.5})$$

We now indentify the appriopiate Reynolds number for the problem as  $Re_g = \rho U \epsilon R/\mu = \rho U H_d/\mu$  on the LHS. We note that if this number is small, we can neglect the terms on the LHS of the equation. Furthermore, since  $\epsilon$  is small, we can neglect higher order terms to obtain:

$$\frac{\partial p^*}{\partial r^*} = \frac{\partial^2 u_r^*}{\partial z^{*2}} \quad (\text{A.6})$$

Back substitution of dimensional variables gives:

$$\frac{\partial p}{\partial r} = \mu \frac{\partial^2 u_r}{\partial z^2} \quad (\text{A.7})$$

A similar analysis for the  $z$ -component of the flow leads to:

$$\frac{\partial p}{\partial z} = 0 \quad (\text{A.8})$$

## Appendix B

# SRYL theory for slow drops

A schematic of a drop approaching a flat surface is depicted in Fig. B.1.

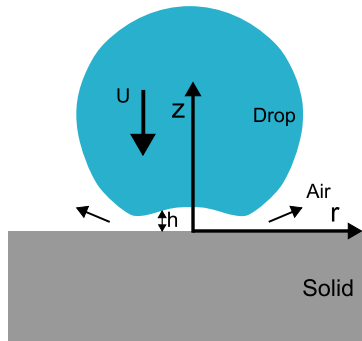


Figure B.1: Schematic of drop impact onto a flat surface. The thin film that is trapped between the drop and the solid is characterized by  $h(r, t)$ .

The pressure in the thin film trapped between a slow impacting drop and the flat plate is given the Young-Laplace equation:

$$p = \frac{2\gamma}{R} - \frac{\gamma}{r} \frac{\partial}{\partial r} \left( r \frac{\partial h}{\partial r} \right). \quad (\text{B.1})$$

Inertial effects are thus neglected, and the pressure in the film is fully determined by the curvature of the interface. The thinning rate of the film is given by the Stokes-Reynolds equation which describes the dynamics of the film:

$$\frac{\partial h}{\partial t} = \frac{1}{12\mu r} \frac{\partial}{\partial r} \left( r h^3 \frac{\partial p}{\partial r} \right). \quad (\text{B.2})$$

Upon inserting Eq. B.1 into Eq. B.2 we obtain an equation with fourth-order derivatives in  $h$ :

$$\frac{\partial h}{\partial t} = \frac{1}{12\mu r} \frac{\partial}{\partial r} \left( r h^3 \frac{\partial}{\partial r} \left( -\frac{\sigma}{r} \frac{\partial}{\partial r} \left( r \frac{\partial h}{\partial r} \right) \right) \right). \quad (\text{B.3})$$

This equation can be solved with the method of lines similar as was done in [34, 35], which effectively turns the PDE equation B.3 into an ODE equation. The following boundary conditions are employed. At  $r = 0$  we have  $\frac{\partial p}{\partial r} = 0 = \frac{\partial h}{\partial r}$  due to symmetry. For large radial coordinate  $r \rightarrow \infty$ , the excess pressure  $p$  has to go to zero, since there will be no pressure build up far away from the impact zone. It has been shown theoretically [36] that  $p$  decays as  $p \sim r^{-4}$ . This boundary condition will be implemented, rather than simply putting the  $p = 0$  at a large radial coordinate [34, 35]. The boundary condition  $p \sim r^{-4}$  is implemented as  $r \frac{\partial p}{\partial r} + 4p = 0$  for  $r \rightarrow \infty$ . Furthermore, at some large radial coordinate  $r = r_{max}$ , the interface moves with a set impact velocity:  $\frac{\partial h}{\partial t} = -V(t)$ . As an initial condition a parabolic shape for the impacting drop will be assumed:  $h(r, 0) = h_0 + r^2/2R_0$ , which gives indeed zero excess pressure when applying Eq. B.1 to this initial geometry. Here  $h_0$  is some initial separation where the drop doesn't feel

the wall yet, this is practically taken as  $h_0 = 50 \mu m$ . Equation B.3 can be nondimensionalized [17] by adopting the following dimensionless variables:

$$p' = \frac{R}{\sigma} p \quad t' = Ca^{1/2} \frac{\sigma}{R\mu} t \quad r' = Ca^{-1/4} \frac{r}{R} \quad h' = Ca^{-1/2} \frac{h}{R}$$

We can now write Eq. B.3 in terms of these nondimensional variables:

$$\frac{\partial h'}{\partial t'} = \frac{1}{12r'} \frac{\partial}{\partial r'} \left( r' h'^3 \frac{\partial}{\partial r'} \left( -\frac{1}{r'} \frac{\partial}{\partial r'} \left( r' \frac{\partial h'}{\partial r'} \right) \right) \right). \quad (\text{B.4})$$

From the dimensionless variables that were used to successfully nondimensionalize Eq. B.3 we can already deduce that:  $\frac{H_d}{R} \sim \sqrt{Ca}$  and  $\frac{V_b}{R^3} \sim Ca$ . Because we plot our results in terms of  $St$ , let us convert these scaling in terms of  $St$ : For  $H_d$  this becomes:

$$\frac{H_d}{R} \sim \sqrt{Ca} \sim \sqrt{(We/St)} \sim \frac{\mu_g}{\sqrt{\gamma \rho_l R}} St^{1/2} \quad (\text{B.5})$$

And for  $V_b$  this becomes [9]:

$$\frac{V_b}{R^3} \sim Ca \sim We/St \sim \frac{\mu_g^2}{\gamma \rho_l R} St \quad (\text{B.6})$$

We note that the scaling suggested by SRYL is indeed the same as was derived by Bouwhuis et al. [16]. We now have a look at a typical simulation result, which is depicted in Fig. B.2. As we can see from this time evolution  $H_d$  converges during impact, which has been confirmed by some stability tests. No real bubble volume can be determined yet though, since the drop is not enclosing any air yet. As we can also see, the drop keeps spreading without stopping. This is because we have no boundary condition at  $r = r_{max}$  which limits the drops from spreading when it is impacting. While the inner problem of drop impact is solved, there is not yet a connection to the outer drop shape which guarantees volume conservation, and what would prevent the drop from spreading. In practice this would mean that the drop keeps spreading, which is not realistic. This can be noted in the final stage of the simulation, which is shown in red, see Fig. B.2. Here the drop has spread to such an extent that the location of  $r_{max}$  can not be regarded as a location far away from the impact zone anymore, which is especially notable in the pressure plot Fig. B.2b. Further increasing the location of  $r_{max}$  is not solving this problem. It is however possible to solve this problem by matching the inner solution at the impact zone to the outer drop shape [30], but this is not within the scope of the present thesis.

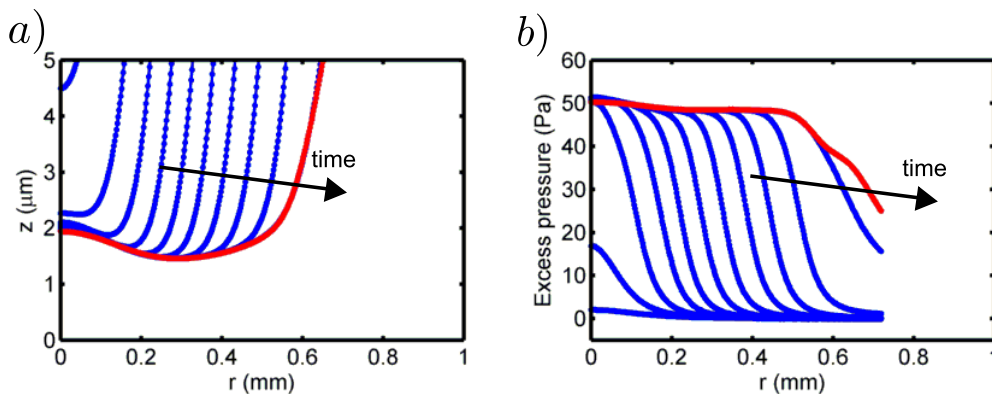


Figure B.2: a) Drop impact based on SRYL theory. Lines are separated by  $0.07 ms$ . To match the results of Bouwhuis et al. the radius is taken  $R = 0.9 mm$ , and the surface tension is set to  $\gamma = 0.022 N/m$ . The impact speed  $U$  is  $U = 0.021 m/s$ . The location of  $r_{max}$  is chosen at  $r_{max} = 0.8R = 0.72 mm$ . b) Corresponding pressure development in the draining air film.

As the dimple height  $H_d$  is already converged, we can compare this value with the already existing results of Bouwhuis et al. [9], see Fig. B.3. We find excellent agreement in both comparison to experiments, existing BIM results and theory which predicts  $H_d/R \sim St^{1/2}$ . It is worth noting that SRYL theory can be further developed to study the discrepancy in  $V_b$  as is explained in Chapter 2 for the capillary regime,

since no inertia of the fluid is taken into account in this model. See also Fig. B.3. This also brings a computational advantage when comparing SRYL to BIM in the capillary regime. A SRYL simulation takes typically minutes, while a BIM simulation in the capillary regime typically takes days.

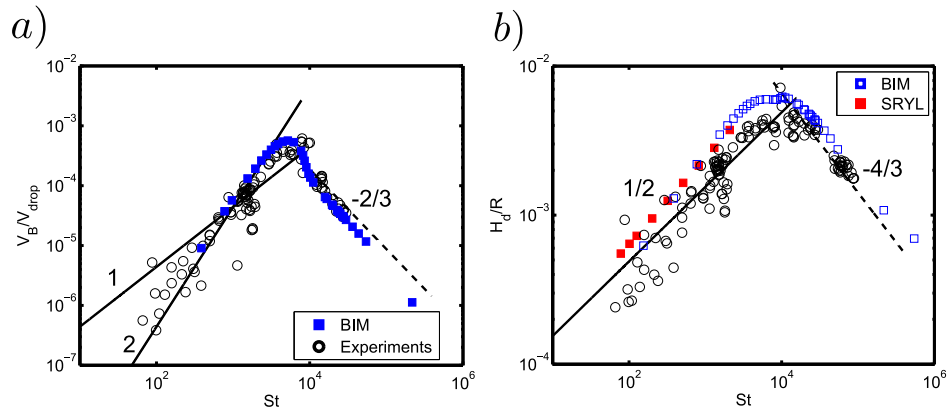


Figure B.3: a) Adapted from Bouwhuis et al. [9]. a) Normalized bubble volume  $V_b/V_{drop}$  versus  $St$ . Blue symbols correspond to BIM results, black open circles correspond to experimental data. b) Normalized dimple height  $H_d/R$  versus  $St$ . SRYL results are superimposed on existing experimental and BIM data and show excellent agreement.

# Acknowledgments

First of all I want to thank my daily supervisor Wilco Bouwhuis for his guidance throughout the whole project. He proved to be a good mentor, and helped me to get started real quickly with a subject that I had no experience with before. Wilco spend a lot of time with me on the project, and the result would not be as it is without his help and guidance. He could motivate me at the right time when I needed it. I also want to thank Jacco Snoeijer for his guidance during the project. I think it is impressive that even though you don't run the BIM simulations yourself, your insight in the problems we faced is big. During efficient meetings you were able to identify the core of a problem that I encountered quickly, and helped me towards the right direction. Apart from that you proved to be also very motivating. I want to thank Detlef Lohse for letting me do research in such a fantastic group. You were also very supportive in letting me do both numerics and experiments, a freedom and trust that I really appreciate. I want to thank Peichun Amy Tsai for making me enthusiast about doing research during my first real science project, the BSc. assignment. With no experience in such a project beforehand, you were always inspiring me to go for the extra mile, which eventually resulted in a scientific publication which inspired me in future projects such as my MSc. project. It is nice that you came with the idea of a new experimental collaboration project during my master project. Though the main focus of my work is on numerics, I enjoyed working on this exciting experimental project, which is also part of this thesis. This leads me immediately to Roeland van der Veen, from who I learned to perform the high-speed color interferometry method which was needed in the experimental project. He guided me with experiments, and we had nice discussions about the data interpretation. Also, he was willing to help me with his Matlab skills when I was making the 3d animation of my simulation results, from which a snapshot is used for the cover picture of this thesis. It would definitely not look as good without your help. I want to thank Devaraj van der Meer for useful discussions we had, for example in the beginning of the project, where we struggled to implement two liquid domains instead of one in our numerical code. I also want to thank Marc Dhallé for taking a place in my commmittee as an external member. I also want to thank Rodrigo Ezeta and Mahening Citravidya for the nice collaboration we had in the lab during your Experimental Technique project which was related to my Master project. I also want to thank Rik Groenen for taking the SEM images of the micro structures that were used for experiments.

I want to thank Mike and Sam for being around right from the start of our studies, and for the support during hard times. Its fantastic to spend time with you, and I'm sure we keep in touch even though we may not be living in the same city anymore. I want to thank my fellow Bracquers for all the adventures and fun throughout my studies, and also for the support. I want to thank my roommates from Huize A-A-A3 for the fun and support during the last 2 years I lived with you. I also would like thank my roommates from the student room. Though it could be quite noisy with about twelve students in one room, the high quality of the jokes definitely compensated for this. I want to thank my parents and family for continuing support throughout my whole studies. You have always been very supportive. This means a lot to me.

Enschede, June 2013

# References

- [1] A. M. Worthington and R. S. Cole. Impact with a liquid surface studied by the aid of instantaneous photography. *Phil. Trans. R. Soc. Lond. A*, 189:137–148, 1897.
- [2] A. M. Worthington and R. S. Cole. Impact with a liquid surface studied by the aid of instantaneous photography. *Phil. Trans. R. Soc. Lond. A*, 194:175–199, 1900.
- [3] J. O. Marston, I. U. Vakarelski, and S. T. Thoroddsen. Bubble entrapment during sphere impact onto quiescent liquid surfaces. *Journal of Fluid Mechanics*, 680:660–670, 2011.
- [4] M. Do-Quang and G. Amberg. The splash of a solid sphere impacting on a liquid surface: Numerical simulation of the influence of wetting. *Physics of Fluids*, 21(2), 2009.
- [5] Q. Deng, A. V. Anilkumar, and T. G. Wang. The phenomenon of bubble entrapment during capsule formation. *Journal of colloid and interface science*, 333(2):523–532, 2009.
- [6] T. Tran, H. Maleprade, C. Sun, and D. Lohse. Air entrainment during impact of droplets on liquid surfaces. *Journal of Fluid Mechanics*, 726, 2013.
- [7] S. T. Thoroddsen, M. J. Thoraval, K. Takehara, and T. G. Etoh. Micro-bubble morphologies following drop impacts onto a pool surface. *Journal of Fluid Mechanics*, 708:469–479, 2012.
- [8] D. B. van Dam and C. Le Clerc. Experimental study of the impact of an ink-jet printed droplet on a solid substrate. *Physics of Fluids*, 16(9):3403–3414, 2004.
- [9] W. Bouwhuis, R. C. A. Van Der Veen, T. Tran, D. L. Keij, K. G. Winkels, I. R. Peters, D. Van Der Meer, C. Sun, J. H. Snoeijer, and D. Lohse. Maximal air bubble entrainment at liquid-drop impact. *Physical Review Letters*, 109(26), 2012.
- [10] R. C. A. Van Der Veen, T. Tran, D. Lohse, and C. Sun. Direct measurements of air layer profiles under impacting droplets using high-speed color interferometry. *Physical Review E - Statistical, Nonlinear, and Soft Matter Physics*, 85(2), 2012.
- [11] A. H. . Cheng and D. T. Cheng. Heritage and early history of the boundary element method. *Engineering Analysis with Boundary Elements*, 29(3):268–302, 2005.
- [12] S. Gekle. *Introductory literature about Boundary Integral in general*. University of Twente, 2010.
- [13] P.K. Kundu and I.A. Cohen. *Fluid Mechanics*. Elsevier Academic Press, 2004.
- [14] C. Pozrikidis. *Introduction to theoretical and computational fluid dynamics*. Oxford University Press, 1997.
- [15] E. Klaseboer, Q. Sun, and D. Y. C. Chan. Non-singular boundary integral methods for fluid mechanics applications. *Journal of Fluid Mechanics*, 696:468–478, 2012.
- [16] W. Bouwhuis. Modeling the instability of droplets floating on an airflow. *MSc. thesis, University of Twente, Physics of Fluids group*, 2011.
- [17] E. Klaseboer, J. P. Chevallier, C. Gourdon, and O. Masbernat. Film drainage between colliding drops at constant approach velocity: Experiments and modeling. *Journal of colloid and interface science*, 229(1):274–285, 2000.
- [18] P. D. Hicks and R. Purvis. Air cushioning and bubble entrapment in three-dimensional droplet impacts. *Journal of Fluid Mechanics*, 649:135–163, 2010.

- [19] S. Mandre and M. P. Brenner. The mechanism of a splash on a dry solid surface. *Journal of Fluid Mechanics*, 690:148–172, 2012.
- [20] R. Ezeta and M. Citravidya. *Droplet Impact on a Liquid Surface, Experimental Technique course*. University of Twente, Physics of Fluids group, 2013.
- [21] Y. Couder, E. Fort, C. . Gautier, and A. Boudaoud. From bouncing to floating: Noncoalescence of drops on a fluid bath. *Physical Review Letters*, 94(17), 2005.
- [22] J. R. Saylor and G. D. Bounds. Experimental study of the role of the weber and capillary numbers on mesler entrainment. *AIChE Journal*, 58(12):3841–3851, 2012.
- [23] R. C. A. Van Der Veen, M. H. W. Hendrix, T. Tran, P. Tsai, C. Sun, and D. Lohse. Air film dynamics during drop impact onto hydrophobic micro-patterned surfaces. *Work in preparation for submitting to PRL*, 2013.
- [24] S. Mandre, M. Mani, and M. P. Brenner. Precursors to splashing of liquid droplets on a solid surface. *Physical Review Letters*, 102(13), 2009.
- [25] M. Mani, S. Mandre, and M. P. Brenner. Events before droplet splashing on a solid surface. *Journal of Fluid Mechanics*, 647:163–185, 2010.
- [26] J. S. Lee, B. M. Weon, J. H. Je, and K. Fezzaa. How does an air film evolve into a bubble during drop impact? *Physical Review Letters*, 109, 2012.
- [27] L. Xu, W. W. Zhang, and S. R. Nagel. Drop splashing on a dry smooth surface. *Physical Review Letters*, 94(18), 2005.
- [28] P. Tsai, M. H. W. Hendrix, R. R. M. Dijkstra, L. Shui, and D. Lohse. Microscopic structure influencing macroscopic splash at high weber number. *Soft Matter*, 7(24):11325–11333, 2011.
- [29] H. V. Jansen, J. G. E. Gardeniers, J. Elders, H. A. C. Tilmans, and M. Elwenspoek. Applications of fluorocarbon polymers in micromechanics and micromachining. *Sensors and Actuators: A.Physical*, 41(1-3):136–140, 1994.
- [30] D. Y. C. Chan, E. Klaseboer, and R. Manica. Theory of non-equilibrium force measurements involving deformable drops and bubbles. *Advances in Colloid and Interface Science*, 165(2):70–90, 2011.
- [31] S. Popinet. Gerris: A tree-based adaptive solver for the incompressible euler equations in complex geometries. *Journal of Computational Physics*, 190(2):572–600, 2003.
- [32] V. Kumaran. *Lecture notes Transport Phenomena*. Indian Institute of Science, 2013.
- [33] M.M. Denn. *Process Fluid Mechanics*. Prentice Hall, 1980.
- [34] M. H. W. Hendrix, R. Manica, E. Klaseboer, D. Y. C. Chan, and C. D. Ohl. Spatiotemporal evolution of thin liquid films during impact of water bubbles on glass on a micrometer to nanometer scale. *Physical Review Letters*, 108(24), 2012.
- [35] D. Y. C. Chan, E. Klaseboer, and R. Manica. Film drainage and coalescence between deformable drops and bubbles. *Soft Matter*, 7(6):2235–2264, 2011.
- [36] S. G. Yiantsios and R. H. Davis. On the buoyancy-driven motion of a drop towards a rigid surface or a deformable interface. *Journal of Fluid Mechanics*, 217:547–573, 1990.